

# Chapter 7

## Nonequilibrium Energy Transfer in Nanostructures



Fourier's law and the associated heat diffusion equation comprise one of the most celebrated models in mathematical physics. Joseph Fourier in 1824 wrote: *Heat, like gravity, penetrates every substance of the universe; its rays occupy all parts of space. ...The theory of heat will hereafter form one of the most important branches of general physics.* Soon afterward, heat transfer also became an important engineering field, essential to the second industrial revolution and the development of modern technologies.

Recall the discussion of heat interaction and heat transfer in Chap. 2. We have treated heat conduction as a diffusion process based on the concept of local thermal equilibrium. This allows us to define and determine the equilibrium temperature at each location in a body instantaneously, under the continuum assumption described in Chap. 1. The local-equilibrium condition breaks down at the microscale when the characteristic length  $L$  is smaller than a mechanistic length scale, such as the mean free path  $\Lambda$ . For conduction by molecules, consider a rarefied gas between two parallel plates at different temperatures. If the mean free path is much greater than the separation distance, i.e., the Knudsen number  $Kn = \Lambda/L \gg 1$ , the gas is in the free molecule regime and its velocity distribution cannot be described by Maxwell's distribution function. Furthermore, the transport becomes ballistic rather than diffusive. Nonequilibrium energy transfer refers to the situation when the assumption of local equilibrium does not hold. This can occur in solid nanostructures even at room temperature and in a steady state, or in bulk solids under the influence of short pulse heating.

For heat conduction *across* a dielectric thin film, when the thickness is much smaller than the phonon mean free path, which increases as the temperature goes down, the condition of local equilibrium is not satisfied. Hence, the phonon statistics at a given location cannot be described by the equilibrium distribution function at any given temperature. Strictly speaking, temperature cannot be defined inside the medium. However, an *effective* temperature is typically adopted, based on the statistical average of the particle energies. In the case of heat transfer across a thin

dielectric film or between two plates separated by a rarefied molecular gas, the effective temperature distribution cannot be described by the heat diffusion theory derived from Fourier's law, using the concept of equilibrium temperature without considering the temperature jumps at the boundaries. The concept of temperature jump was introduced in Chap. 4 (e.g., Fig. 4.12). Consider a metal or a superconductor that is subjected to ultrafast pulsed laser heating, in which the pulse duration may range from several femtoseconds to a few nanoseconds. The electrons gain energy quickly to reach a state that is far from equilibrium with the crystal lattice or the phonon system. The transport processes during and immediately after the laser pulse become nonequilibrium both temporally and spatially. Conventional Fourier's law cannot be directly applied.

In Chap. 5, we have considered the size effect on thermal transport in solids. Two approaches have been used under different situations. In the first situation, we apply Matthiessen's rule to account for the reduction in mean free path by assuming that Fourier's law is still applicable but with a size-dependent thermal conductivity. In the second situation, where the transport is completely ballistic, we use the concept of quantum conductance based on the Landauer formulation to solve the problem in a straightforward manner. The definition of an effective thermal conductivity is particularly useful for the study of transport processes *along* a thin film or a thin wire, when the length in the direction of transport is much greater than the mean free path. In this case, a local equilibrium can be established, and thus, the energy transfer is well described by Fourier's law, even though the thickness is less than the mean free path. Here, the only microscale effect is the classical size effect, which arises from boundary scattering of electrons in a metal or phonons in an insulator or a semiconductor. For energy transport across a thin film or in a multilayer structure, on the other hand, the local-equilibrium condition breaks down when the film thickness is much smaller than the mean free path. Furthermore, thermal boundary resistance (TBR) may become significant at the interfaces. Because of the wave-particle duality, the electron wave or phonon wave effect may need to be considered in some cases. For nonmetallic crystalline materials, the most commonly used method to study thermal transport is based on the Boltzmann transport equation (BTE) of phonons. Various assumptions and techniques have been developed to solve the phonon BTE. In very small structures, such as nanotubes or nanowires, molecular dynamics (MD) and other atomistic simulation methods may be more suitable.

This chapter begins with a description of the phenomenological theories in which the energy transport processes are represented by a single differential equation or a set of differential equations that can be solved with appropriate initial and boundary conditions. These equations are often called non-Fourier heat equations, which can be considered as extensions of the conventional heat diffusion equation based on Fourier's law. The limitations of the phenomenological theories are discussed. While the BTE, Monte Carlo method, and MD simulations have been presented in previous chapters, this chapter stresses the application in solid nanostructures, including thermal boundary resistance (TBR) and multilayer structures. The equation of phonon radiative transfer (EPRT) is introduced and used to delineate the diffusive and ballistic heat conduction regimes in thin films. A heat conduction regime with

respect to length and time scale is presented, followed by a summary of the contemporary methods for measuring thermal transport properties of solids, thin films, and nanostructures.

## 7.1 Phenomenological Theories

A fundamental difficulty of Fourier's heat conduction theory was thought to be that a thermal disturbance in one location of the medium would cause a response at any other location instantaneously, as required by the mathematical solution of the diffusion equation. In theory, the speed of heat propagation appears to be unlimited; this has been viewed by some as a direct violation of the principle of causality. Let us begin with an example of 1D transient heating of a semi-infinite medium. Assume that the medium is homogeneous, with constant thermal properties, and is initially at a uniform temperature  $T(x, 0) = T_i$ . The thermal diffusivity of the medium is  $\alpha = \kappa/(\rho c_p)$ , where  $\kappa$ ,  $\rho$ , and  $c_p$  are the thermal conductivity, density, and specific heat of the material, respectively. The wall at  $x = 0$  is heated with a constant heat flux  $q_0''$  at  $0 < t \leq t_p$ , where  $t_p$  is the width of the step heating, and insulated at  $t > t_p$ . The solution of the temperature distribution  $T(x, t)$  can be found from Refs. [1, 2] as follows:

$$T(x, t) - T_i = 2q_0'' \frac{\sqrt{\alpha t}}{\kappa} F(\xi) \text{ at } 0 < t \leq t_p \quad (7.1a)$$

$$T(x, t) - T_i = 2q_0'' \frac{\sqrt{\alpha t}}{\kappa} \left[ F(\xi) - \eta F\left(\frac{\xi}{\eta}\right) \right] \text{ at } t > t_p \quad (7.1b)$$

where  $\xi = x/\sqrt{4\alpha t}$ ,  $\eta = \sqrt{1 - t_p/t}$ , and  $F(\xi) = \pi^{-1/2} \exp(-\xi^2) - \xi \operatorname{erfc}(\xi)$  with  $\operatorname{erfc}$  being the complementary error function as given in Appendix B.1.2. While  $F(10) = 2.1 \times 10^{-44}$  and the right-hand sides of both Eqs. (7.1a) and (7.1b) are essentially negligible when  $x > 3\sqrt{\alpha t}$ , the paradox is that a nonzero response must not occur faster than the speed of the thermal energy carriers, such as the Fermi velocity in metals or the speed of sound in dielectrics. In reality, this rarely causes any problem because a signal that is below the noise level cannot be detected by any physical instrument, as will be discussed in the example next.

**Example 7.1** A thick plate of fused silica  $\text{SiO}_2$ , initially at room temperature, is heated at one surface by a heat flux of  $10^5 \text{ W/m}^2$  for 5 s and then insulated. Treat the heated surface to be at  $x = 0$ , and assume the other surface is at  $x \rightarrow \infty$ . Plot the temperature distributions at various times. Imagine a temperature sensor is placed at certain locations with instantaneous response and zero additional heat capacity. Estimate the time for the thermometer to sense the temperature rise as a function of the location  $x$ . Assume that the thermophysical properties of the glass are constant,  $\kappa = 1.4 \text{ W/m K}$ , and  $\alpha = 8.5 \times 10^{-7} \text{ m}^2/\text{s}$ .

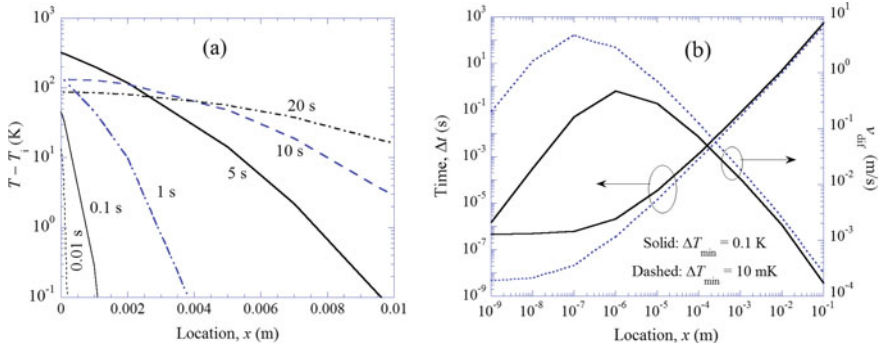


**Fig. 7.1** **a** The temperature distributions at various times. **b** The time required for a given location to acquire a minimum temperature rise and the estimated thermal diffusion speed

**Solution** The temperature distribution is shown in Fig. 7.1a at  $t = 0.01, 0.1, 1, 5, 10,$  and  $20$  s. During the heating, the temperature monotonically increases with time and the heat flux is always positive. After the heat input is stopped when  $t = 5$  s, the temperature near the surface decreases but is still the highest and the temperature decreases toward increasing  $x$ . While the predicted temperature rises everywhere instantaneously, the magnitude may be too small to be observed practically. We can calculate the time  $\Delta t$  required for a minimum temperature rise  $\Delta T_{\min}$ , specified by the thermometer sensitivity. Let us choose  $\Delta T_{\min} = 10$  mK and  $0.1$  K for illustration. The *average thermal diffusion speed* can be estimated by  $v_{\text{dif}}(x) = x/\Delta t$ , for any given location  $x$ . The results are shown in Fig. 7.1b. In reality, diffusion is often a slow process near room temperature. For the example given here,  $v_{\text{dif}}$  for  $\Delta T_{\min} = 10$  mK is between  $1$  and  $5$  m/s, for  $5$  nm  $< x < 5$   $\mu\text{m}$ , and goes down rapidly at  $x > 5$   $\mu\text{m}$ . At  $x = 10$  mm,  $v_{\text{dif}}$  is only  $2$ – $3$  mm/s. On the other hand, the speed of sound in glass is on the order of  $5$  km/s, which is several orders of magnitude greater than the average thermal diffusion speed.

Recall that the uncertainty principle in quantum mechanics states that  $\Delta E \Delta t > \hbar$ , suggesting that we cannot measure time and energy simultaneously with unlimited precision. From statistical mechanics, the distribution function allows a small fraction of particles to have a very high speed or to travel a very large distance without collision, although the probability may be extremely low. Based on the uncertainty principle and statistical mechanics, it seems convincing that Fourier’s law, in its applicable regime, does not violate the principle of causality. What is physically problematic and practically impossible is to provide a temperature impulse to the surface or at any given location instantaneously. We further conclude that the heat diffusion equation does not produce an infinite speed of thermal energy propagation; rather, it is often a very slow process. Microscopically, Fourier’s law fails when a local equilibrium is not established, as explained earlier. At the same time, the concept of an equilibrium temperature cannot be applied. It is critically important

for the technological advancement to establish and apply thermal transport theories, both microscopically and macroscopically, under nonequilibrium conditions.

Several phenomenological theories have been developed to describe transient heat transfer processes in solids and micro/nanostructures. Applications of transient and ultrafast heating include laser processing, nanothermal fabrication, and the measurement of thermophysical properties. In the literature, there appears to be controversial experimental evidence on the existence of certain phenomena predicted by the hyperbolic heat conduction [3]. Furthermore, a large division exists as regards the formulation and the interpretation of the theories of non-Fourier conduction. While the intention is to provide a clear and objective presentation, the discussion will inevitably reflect the author's personal views and limitations at the time when the manuscript was prepared. This section should help readers gain a general understanding of the basic concepts and phenomena related to non-Fourier heat conduction. Although relatively few papers out of a large number of publications are cited in the text and the reference section, interested readers can easily trace the relevant literature from the cited sources, especially Refs. [3–6].

### 7.1.1 Hyperbolic Heat Equation

Several earlier studies have pointed out that the instantaneous response may be an indication of a nonphysical feature of the Fourier heat theory. Carlo Cattaneo in 1948 used kinetic theory of gas to derive a rate equation given by

$$\mathbf{q}''(\mathbf{r}, t) + \tau_q \frac{\partial \mathbf{q}''(\mathbf{r}, t)}{\partial t} = -\kappa \nabla T(\mathbf{r}, t) \quad (7.2)$$

which is a *modified Fourier equation* called *Cattaneo's equation*. The historical contributions by James Clerk Maxwell in 1867 and Pierre Vernotte in 1958 have been extensively reviewed by Joseph and Preziosi [4] and will not be repeated here. In Eq. (7.2),  $\tau_q$  is a kind of relaxation time, originally thought to be the same as  $\tau$ , i.e., the average time between collisions. The energy equation for heat conduction involving an internal source or volumetric heat generation rate  $\dot{q}(\mathbf{r}, t)$  is

$$\dot{q}(\mathbf{r}, t) - \nabla \cdot \mathbf{q}''(\mathbf{r}, t) = \rho c_p \frac{\partial T(\mathbf{r}, t)}{\partial t} \quad (7.3)$$

The divergence of Eq. (7.2) and the time derivative of Eq. (7.3) give two new equations, which can be combined with Eq. (7.3) to eliminate the heat flux terms. The resulting differential equation for constant properties can be written as

$$\frac{\dot{q}}{\kappa} + \frac{\tau_q}{\kappa} \frac{\partial \dot{q}}{\partial t} + \nabla^2 T = \frac{1}{\alpha} \frac{\partial T}{\partial t} + \frac{\tau_q}{\alpha} \frac{\partial^2 T}{\partial t^2} \quad (7.4)$$

This is the *hyperbolic heat equation*, in contrast to the heat diffusion equation or parabolic heat equation. Without heat generation, we can rewrite Eq. (7.4) as

$$\nabla^2 T = \frac{1}{\alpha} \frac{\partial T}{\partial t} + \frac{1}{v_{tw}^2} \frac{\partial^2 T}{\partial t^2} \quad (7.5)$$

which is a telegraph equation or a damped wave equation. The solution of the hyperbolic heat equation results in a propagating wave, the amplitude of which decays exponentially as it travels. The speed of this *temperature wave* in the high-frequency limit, or the short-time limit, is given by

$$v_{tw} = \sqrt{\alpha/\tau_q} \quad (7.6)$$

The amplitude of the temperature wave decays according to  $\exp(-t/\tau_q)$  due to the damping caused by the first-order time-derivative term  $(1/\alpha)(\partial T/\partial t)$ , which is also called the diffusion term. For an insulator, from the simple kinetic theory we have  $\kappa = \frac{1}{3}(\rho c_v)v_g^2\tau$ . Noting that  $c_v = c_p$  for an incompressible solid and assuming  $\tau_q = \tau$ , we get

$$v_{tw} = v_g/\sqrt{3} \quad (7.7)$$

Equation (7.7) relates the speed of the temperature wave to the speed of sound in an insulator. The square root of three can be understood as due to the randomness of thermal fluctuations in a 3D medium, just like the relation between the velocity and its components,  $\overline{v^2} = \overline{v_x^2} + \overline{v_y^2} + \overline{v_z^2}$ , in kinetic theory. Earlier experiments at cryogenic temperatures have demonstrated a second sound propagating at the velocity  $v_{2nd} = v_g/\sqrt{3}$  in liquid helium and some solids [4].

Equation (7.5) sets a limit on the heat propagation speed, which is manifested by a sharp wavelike behavior that travels at  $v_{tw}$  inside the medium for a sudden temperature change at the boundary. As a wave equation, the solution of the temperature has an amplitude and a phase. Theoretically, the temperature wave can be reflected by another boundary and can interfere, constructively or destructively, with a forward propagating wave. The interaction between the temperature waves may also result in a resonance effect, a typical wave phenomenon. Numerous analytical and numerical predictions have been made [6–10]. It should be noted that the terms *heat wave* [4] and *thermal wave* [7] have also been frequently used in the literature to describe the temperature wave behavior. The term “temperature wave” is used in this chapter for the wavelike behavior associated with the hyperbolic-type heat equations, because “heat wave” might be confused with the calamitous weather phenomenon and “thermal wave” might be confused with the diffusion wave used in photoacoustic techniques. Bennett and Patty [11] clarified: *The term thermal wave interference is used to mean the superposition of simple harmonic solutions of the thermal diffusion equation. Although wavelike in nature there are important differences between thermal waves arising from a differential equation that is of the first order in time*

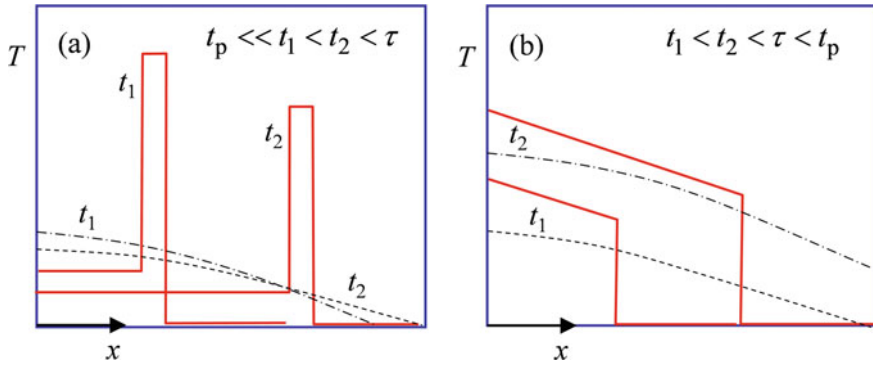


**Fig. 7.2** (Not to scale) Illustration of the solution of the hyperbolic heat equation at short timescales. **a** A short pulse,  $t_p \ll \tau$ . **b** A long pulse,  $t_p > \tau$ . The solid curves are the solutions of the hyperbolic heat equation (7.5), and the dash-dotted and dashed curves are the solutions of the heat diffusion equation (7.1a, 7.1b)

and waves that are solution to a wave equation that is of the second order in time. In the heat transfer literature, thermal wave often refers to periodic-heating techniques used widely for thermophysical property measurements [12].

Let us consider an example of a semi-infinite solid under a constant heat flux at the surface. Figure 7.2 illustrates the solutions for a small  $t_p$  and a large  $t_p$ , compared with  $\tau$ . Here again, we have assumed  $\tau_q = \tau$ . The propagation speed is equal to  $v_{tw}$ , and the pulse wavefront is given by  $x_1 = v_{tw}t_1$  and  $x_2 = v_{tw}t_2$ . Hence,  $x_1 < x_2 < \Lambda$ , where  $\Lambda = v_g\tau$  is the mean free path. In the case of a short pulse, the temperature pulse propagates and its height decays by dissipating its energy to the medium as it travels. The parabolic heat equation, on the other hand, predicts a continuous temperature distribution without any wavefront (see Fig. 7.2).

As time passes on, the first-order time derivative, or the diffusion term, in Eq. (7.5) dominates. If the relative change of  $\partial T/\partial t$  or  $\mathbf{q}''$  during one  $\tau_q$  is large, then the wave feature is important. This should happen immediately after a sudden thermal disturbance that results in a temporal nonequilibrium, as well as a spatial nonequilibrium near the heat pulse or the wavefront. After a sufficiently long time, usually 5–10 times  $\tau_q$ , a local equilibrium will be reestablished, and the thermal field can be described by the parabolic heat equation. At steady state, the hyperbolic and parabolic equations predict the same results. While Eq. (7.4) is mathematically more general than the heat diffusion equation, it should not be taken as a correction, or a more realistic theory than the Fourier conduction model, because Cattaneo’s equation has not been justified on a fundamental basis, nor has it been validated by any plausible experiments.

Many researchers have investigated the hyperbolic heat equation based on the second law of thermodynamics [13–15]. It has been found that the hyperbolic heat equation sometimes predicts a negative entropy generation and even allows energy to be transferred from a lower temperature region to a higher temperature region. The entropy generation rate for heat conduction without an internal source can be

calculated by [15]

$$\dot{s}_{\text{gen}} = -\frac{1}{T^2} \mathbf{q}'' \cdot \nabla T = \frac{1}{\kappa T^2} \mathbf{q}'' \cdot \left( \mathbf{q}'' + \tau_q \frac{\partial \mathbf{q}''}{\partial t} \right) \quad (7.8a)$$

The above equation was obtained by setting the energy and entropy balances as follows:

$$\rho \frac{\partial u}{\partial t} = -\nabla \cdot \mathbf{q}'' \quad \text{and} \quad \rho \frac{\partial s}{\partial t} = -\nabla \cdot \left( \frac{\mathbf{q}''}{T} \right) + \dot{s}_{\text{gen}} \quad (7.8b)$$

Note that  $du = Tds$ . A negative entropy generation can easily be numerically demonstrated from Eq. (7.5) during the temperature wave propagation. Here, a negative entropy generation does not constitute a violation of the second law of thermodynamics because the concept of “temperature” in the hyperbolic heat equation cannot be interpreted in the conventional sense, due to the lack of local thermal equilibrium. Extended irreversible thermodynamics has been proposed by Jou et al. [16] by modifying the definition of entropy such that it is not a property of the system anymore but also depends on the heat flux vector. The theory of extended irreversible thermodynamics is self-consistent but has not been fully validated by experiments; hence, it cannot be taken as a generalized thermodynamic theory. Similarly, the hyperbolic heat equation should not be treated as a more general theory over Fourier’s heat conduction theory [17].

**Example 7.2** Derive the modified Fourier equation, or Cattaneo’s equation, based on the BTE under the relaxation time approximation.

**Solution** Tavernier [18] first showed that Cattaneo’s equation could be derived for phonons and electrons using the relaxation time approximation of the BTE. As done in Sect. 4.3.2, where we have derived Fourier’s law based on the BTE, let us start by assuming that the temperature gradient is in the  $x$ -direction only. The transient 1D BTE under the relaxation time approximation can be written as follows:

$$\frac{\partial f}{\partial t} + v_x \frac{\partial f}{\partial x} = \frac{f_0 - f}{\tau} \quad (7.9)$$

A further assumption is made such that  $\frac{\partial f}{\partial x} \approx \frac{\partial f_0}{\partial x} = \frac{\partial f_0}{\partial T} \frac{\partial T}{\partial x}$ , which is the condition of local equilibrium. Substitute the local-equilibrium condition into Eq. (7.9) and multiply each term by  $\tau \varepsilon v_x$ . We can then perform integration of each term over the momentum space to obtain

$$\int_{\varpi} \tau \varepsilon v_x \frac{\partial f}{\partial t} d\varpi + \int_{\varpi} \tau \varepsilon v_x^2 \frac{\partial f}{\partial x} d\varpi = \int_{\varpi} \varepsilon v_x f_0 d\varpi - \int_{\varpi} \varepsilon v_x f d\varpi \quad (7.10a)$$

By treating the relaxation time as a constant, applying the local-equilibrium condition to the second term, and noting that the first term on the right-hand side is zero,

we have

$$\tau \frac{\partial q_x''}{\partial t} + \kappa \frac{\partial T}{\partial x} = -q_x'' \text{ or } q_x'' + \tau \frac{\partial q_x''}{\partial t} = -\kappa \frac{\partial T}{\partial x} \tag{7.10b}$$

This equation can be generalized to the 3D case as given in Eq. (7.2), after replacing  $\tau$  with  $\tau_q$ .

The derivation given in this example, however, does *not* provide a microscopic justification of the hyperbolic heat equation, because it is strictly valid only under the local-equilibrium assumption with an averaged relaxation time. The local-equilibrium assumption prohibits application of the derived equation to length scales comparable to or smaller than the mean free path [19, 20]. Suppose a thermal disturbance occurs at a certain time and location; after a duration that is much longer than the relaxation time, Fourier’s law and the parabolic heat equation are well justified because both the spatial and temporal local-equilibrium conditions are met. On the other hand, if we wish to use the modified Fourier equation to study the transient behavior at a timescale less than  $\tau$ , then the disturbance will propagate by a distance shorter than the mean free path, as shown in Fig. 7.2. Therefore, the derivation based on the BTE, under local-equilibrium and relaxation time approximations, is not a microscopic proof of the hyperbolic heat equation, which is meaningful only in a nonequilibrium situation. To this end, it appears that Maxwell in 1867 made the right choice in dropping terms involving the relaxation time in the paper, by assessing that the rate of conduction will rapidly establish itself [3, 4].

Rigorously speaking, the local-equilibrium condition can be expressed in terms of integration, i.e.,

$$\left| \int_{\varpi} \tau v_x^2 \frac{\partial}{\partial x} (f - f_0) \varepsilon d\varpi \right| \ll \left| \kappa \frac{\partial T}{\partial x} \right| \tag{7.11}$$

In deriving Eq. (7.10b), we have loosely assumed  $\int_{\varpi} \tau \varepsilon v_x \frac{\partial f}{\partial t} d\varpi = \frac{\partial}{\partial t} \int_{\varpi} \tau \varepsilon v_x f d\varpi = \tau \frac{\partial q_x''}{\partial t}$ . After a careful examination of the derivations, Zhang et al. [17] noted that Eq. (7.10a) can be rearranged to obtain the following expression:

$$\int_{\varpi} \tau \varepsilon v_x \left( \frac{\partial}{\partial t} + v_x \frac{\partial}{\partial x} \right) (f - f_0) d\varpi + \kappa \frac{\partial T}{\partial x} = -q_x'' \tag{7.12}$$

One may define a new local-equilibrium condition as follows:

$$\left| \int_{\varpi} \tau \varepsilon v_x \frac{D}{Dt} (f - f_0) d\varpi \right| \ll \left| \kappa \frac{\partial T}{\partial x} \right| \tag{7.13}$$

where the operator  $\frac{D}{Dt} = \frac{\partial}{\partial t} + v_x \frac{\partial}{\partial x}$  in the 1D case and can be generalized to 3D cases. With the new local-equilibrium condition, Eq. (7.12) becomes Fourier's law. Therefore, we can derive Fourier's law directly from the BTE even in the transient situation [17]. Based on the above discussion, Fourier's law is not an approximation of Cattaneo's equation. Hence, one should not treat Cattaneo's equation as a generalized Fourier's law. It may be more appropriate to name Eq. (7.2) and the like as modified Fourier's equations.

Without knowing the heat carrier types and statistics, it is impossible to compare Eqs. (7.11) and (7.13). Both assumptions will break down when the smallest geometric dimension is on the same order or smaller than the mean free path. The basic assumption in the relaxation time approximation is that the distribution function is not too far from equilibrium. For a heat pulse with a duration less than  $\tau_p$ , the relaxation time approximation should generally be applied when the time duration  $t > 3\tau_p$ , regardless of whether we are dealing with a thin film or a semi-infinite medium. Atomistic simulations, based on molecular dynamics and the lattice Boltzmann method, have provided further evidence that the hyperbolic heat equation is not applicable at very short timescales or in the nonequilibrium regime, where the applicability of the relaxation time approximation is also questionable [21, 22]. Nevertheless, after some modifications, there exist a number of special cases when the modified heat equation becomes physically plausible and practically applicable. The modified equation does not produce sharp wavefronts like those illustrated in Fig. 7.2.

### 7.1.2 Dual-Phase-Lag Model

Chester [23] first related Cattaneo's equation with a lagging behavior, specifically, there exists a finite buildup time after a temperature gradient is imposed on the specimen for the onset of a heat flow, which does not start instantaneously but rather grows gradually during the initial period on the order of the relaxation time  $\tau$ . Conversely, if the thermal gradient is suddenly removed, there will be a *lag* in the disappearance of the heat current. Gurtin and Pipkin [24] introduced the memory effect to account for the delay of the heat flux with respect to the temperature gradient. They expressed the heat flux as an integration of the temperature gradient over time, in analogy with the stress-strain relationship of viscoelastic materials with instantaneous elasticity. The linearized constitutional equation reads

$$\mathbf{q}''(\mathbf{r}, t) = - \int_{-\infty}^t K(t - t') \nabla T(\mathbf{r}, t') dt' \quad (7.14)$$

where  $K(\xi)$  is a kernel function. Equation (7.14) reduces to Fourier's law when  $K(\xi) = \kappa \delta(\xi)$  and to Cattaneo's equation when  $K(\xi) = (\kappa/\tau_q) e^{-\xi/\tau}$ . By assuming

$$K(\xi) = \kappa_0 \delta(\xi) + \frac{\kappa_1}{\tau_q} e^{-\xi/\tau} \quad (7.15)$$

Joseph and Preziosi [4] showed that the heat flux can be separated into two parts:

$$\mathbf{q}''(\mathbf{r}, t) = -\kappa_0 \nabla T - \frac{\kappa_1}{\tau_q} \int_{-\infty}^t \exp\left(-\frac{t-t'}{\tau_q}\right) \nabla T(\mathbf{r}, t') dt' \quad (7.16a)$$

Hence,

$$\mathbf{q}'' + \tau_q \frac{\partial \mathbf{q}''}{\partial t} = -\kappa \nabla T - \tau_q \kappa_0 \frac{\partial}{\partial t} \nabla T \quad (7.16b)$$

where  $\kappa = \kappa_0 + \kappa_1$  is the steady-state thermal conductivity, as can be seen from Eq. (7.16a). Combined with Eq. (7.3), the heat equation becomes a partial differential equation,

$$\nabla^2 T + \tau_T \frac{\partial}{\partial t} \nabla^2 T = \frac{1}{\alpha} \frac{\partial T}{\partial t} + \frac{\tau_q}{\alpha} \frac{\partial^2 T}{\partial t^2} \quad (7.17)$$

where  $\tau_T = \tau_q \kappa_0 / \kappa$  is known as the *retardation time*. Unless  $\tau_T = 0$  or  $\kappa_0 = 0$ , Eq. (7.17) maintains the diffusive feature and produces an instantaneous response, albeit small, throughout the medium for an arbitrary thermal disturbance.

In a series of papers published in the 1990s, Tzou extended the lagging concept to a dual-phase-lag model, as described in his monograph first published in 1997 and the second edition in 2015 [6]. The starting point of the dual-phase-lag model is the constitutive relationship,

$$\mathbf{q}''(\mathbf{r}, t + \tau_q) = -\kappa \nabla T(\mathbf{r}, t + \tau_T) \quad (7.18)$$

The introduction of a delay time  $\tau_T$  in Eq. (7.18) implies the existence of a lag in the temperature gradient, with respect to the heat flux driven by an internal or external heat source. The rationale of the phenomenological equation given in Eq. (7.18) was that, in some cases, the heat flux might be viewed as the result of a preceding temperature gradient; in other cases, the temperature gradient might be viewed as the result of a preceding heat flux. The heat flux and the temperature gradient can switch roles in the relationship between “cause” and “effect.” Moreover, both lags might occur simultaneously in certain materials under dramatic thermal disturbances, such as during short-pulse laser heating [6, 7]. These primitive arguments should not be scrutinized rigorously; rather, they are merely thinking instruments to help us gain an intuitive understanding of the heat flux and temperature gradient relationship. After applying the Taylor expansion to both sides of Eq. (7.18) and using the first-order approximation, one immediately obtains

$$\mathbf{q}'' + \tau_q \frac{\partial \mathbf{q}''}{\partial t} = -\kappa \nabla T - \tau_T \kappa \frac{\partial}{\partial t} \nabla T \quad (7.19)$$

which is mathematically identical to Eq. (7.16b), with the substitution of  $\tau_q \kappa_0 = \tau_T \kappa$ . Applying the first-order approximation of Eq. (7.18), one may end up with  $\mathbf{q}'' + (\tau_q - \tau_T) \frac{\partial \mathbf{q}''}{\partial t} = -\kappa \nabla T$ , or  $\mathbf{q}'' = -\kappa \nabla T - (\tau_T - \tau_q) \frac{\partial}{\partial t} \nabla T$ , or even  $\mathbf{q}'' + (\tau_q - \frac{\tau_T}{3}) \frac{\partial \mathbf{q}''}{\partial t} = -\kappa \nabla T - \frac{2\tau_T}{3} \kappa \frac{\partial}{\partial t} \nabla T$ . These equations are merely special cases of Eq. (7.19), after regrouping  $\tau_q$  and  $\tau_T$ . The only requirement for Eq. (7.19) to make logical sense is that both  $\tau_q$  and  $\tau_T$  are nonnegative. The reason that a lag in time has been called a phase lag is perhaps because the temperature field can be viewed as a Fourier transform:  $T(\mathbf{r}, t) = \int_{-\infty}^{\infty} \tilde{T}(\mathbf{r}, \omega) e^{-i\omega t} d\omega$ , where  $\tilde{T}(\mathbf{r}, \omega)$  is the Fourier component at frequency  $\omega$ . The actual phase lag  $\omega \tau_T$  (or  $\omega \tau_q$  for heat flux) depends on the frequency. Equation (7.19) is mathematically more general and has some advantages over Cattaneo's equation. From now on, Eq. (7.17) will be called the *lagging heat equation*. It is straightforward to include the source terms in the lagging heat equation, as well as to treat thermophysical properties as temperature dependent. The solution, however, becomes more and more difficult as the complexity increases. Numerous studies have appeared in the literature on analytical solutions and numerical methods [4, 25–28].

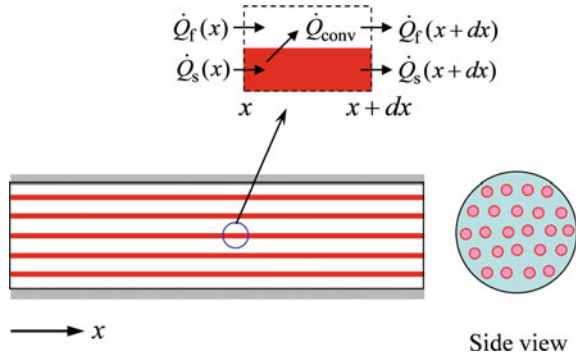
It should be noted that in Eq. (7.15),  $\kappa_0$  and  $\kappa_1$  denote the effective and elastic conductivities, respectively, and are supposed to be nonnegative [4]. Therefore,  $\tau_T$  must not be greater than  $\tau_q$ . In fact, the ratio  $\eta = \kappa_0 / (\kappa_0 + \kappa_1)$  is a direct indication of whether thermal behavior can be described by heat diffusion (when  $\eta = 1$  and  $\kappa_1 = 0$ ) or the hyperbolic heat equation (when  $\eta = 0$  and  $\kappa_0 = 0$ ). In general,  $0 \leq \eta \leq 1$  and the thermal process lies somewhere between the two extremes prescribed by Fourier's law and Cattaneo's equation. In other words, there will be wavelike features in the solution, which is superimposed by an instantaneous diffusive response throughout the medium. The diffusive response here, as well as in Fourier's law, does not correspond to an infinite speed of propagation. Rather, it is well justified by quantum statistics as explained previously.

The dual-phase-lag model relaxes the requirement of  $\tau_T \leq \tau_q$ ; but in the meantime, it produces a negative thermal conductivity component, i.e.,  $\kappa_1 < 0$  according to Eq. (7.15). This drawback has long been overcome by Tzou [6], who proposed a new memory function in accordance with Eq. (7.19) as follows:

$$\mathbf{q}''(\mathbf{r}, t) = -\frac{\kappa}{\tau_q} \int_{-\infty}^t \exp\left(-\frac{t-t'}{\tau_q}\right) \left[ \nabla T(\mathbf{r}, t') + \tau_T \frac{\partial}{\partial t'} \nabla T(\mathbf{r}, t') \right] dt' \quad (7.20)$$

Equation (7.20) suggests that the heat flux depends not only on the history of the temperature gradient but also on the history of the time derivative of  $\nabla T$ . When  $\tau_T = 0$ , Eq. (7.20) becomes Cattaneo's equation. When  $\tau_T = \tau_q$ , Eq. (7.20) reduces to Fourier's law. However,  $\tau_T > \tau_q$  is theoretically permitted because Eq. (7.20) does not presume that the thermal conductivity is composed of an effective conductivity and an elastic conductivity. The inclusion of  $\tau_T > \tau_q$  makes Eq. (7.19) more general than

**Fig. 7.3** Illustration of heat transfer in a solid–fluid heat exchanger, where long solid rods are immersed in a fluid inside a sealed pipe, which is insulated from the outside



the Eq. (7.16a) since this allows the lagging heat equation to describe the behavior of parallel heat conduction that can occur in a number of engineering situations.

Sometimes a microscale phenomenon can be understood easily if a macroscale analogy can be drawn. For this reason, let us consider the solid–fluid heat exchanger shown in Fig. 7.3. Assume that a fluid is stationary inside a sealed pipe, filled with long solid rods. The pipe is insulated from the outside. If the rods are sufficiently thin, we may use the average temperature in a cross section and assume that heat transfer takes place along the  $x$ -direction only. Let us denote the temperatures of the solid rods and the fluid by  $T_s(x, t)$  and  $T_f(x, t)$ , respectively, and take their properties  $\kappa_s, C_s = (\rho c_p)_s, \kappa_f$ , and  $C_f = (\rho c_p)_f$  to be constant. Note that  $C_s$  and  $C_f$  are the *volumetric heat capacities*. Given the rod diameter  $d$ , the number of rods  $N$ , and the inner diameter  $D$  of the pipe, the total surface area per unit length is  $P = N\pi D$ , and the total cross-sectional areas of the rods and the fluid are  $A_c = N\pi d^2/4$  and  $A_f = (\pi/4)(D^2 - Nd^2)$ , respectively. Assume the average convection coefficient is  $h$ . The energy balance equations can be obtained using the control volume analysis as follows:

$$C_s \frac{\partial T_s}{\partial t} = \kappa_s \frac{\partial^2 T_s}{\partial x^2} - G(T_s - T_f) \tag{7.21a}$$

and

$$C_f' \frac{\partial T_f}{\partial t} = G(T_s - T_f) \tag{7.21b}$$

where  $G = hP/A_c$  and  $C_f' = C_f A_f/A_c$ . In writing Eq. (7.21b), we have assumed that  $\kappa_f \ll \kappa_s$  and dropped the term  $\kappa_f \frac{\partial^2 T_f}{\partial x^2}$ . Equations (7.21a) and (7.21b) are coupled equations that can be solved for the prescribed initial and boundary conditions. These are completely macroscopic equations governed by Fourier’s law of heat conduction. Nevertheless, we can combine Eqs. (7.21a) and (7.21b) to eliminate  $T_f$  and, consequently, obtain the following differential equation for  $T_s$ :

$$\frac{\partial^2 T_s}{\partial x^2} + \tau_T \frac{\partial}{\partial t} \left( \frac{\partial^2 T_s}{\partial x^2} \right) = \frac{1}{\alpha} \frac{\partial T_s}{\partial t} + \frac{\tau_q}{\alpha} \frac{\partial^2 T_s}{\partial t^2} \quad (7.22)$$

where  $\alpha = \frac{\kappa_s}{c_s + c_f}$ ,  $\tau_T = \frac{C_f}{G}$ , and  $\tau_q = \frac{C_s \tau_T}{c_s + c_f} < \tau_T$ . The same equation can also be obtained for the fluid temperature  $T_f$ . Here,  $\tau_q$  does not have the meaning of relaxation time. Equation (7.22) is completely physical but should not be viewed as a wave equation; rather, it describes a parallel or coupled heat diffusion process. The concept of dual phase lag can still be applied. It should be noted that, due to the initial temperature difference between the rod and the fluid, a local equilibrium is not established at any  $x$  inside the pipe, until after a sufficiently long time.

Although no fundamental physics can be gained from this example, it can help us appreciate that the lagging heat equation may be useful for describing the behavior in inhomogeneous media. Minkowycz et al. [29] studied the heat transfer in porous media by considering the departure from local thermal equilibrium and obtained higher order differential equations similar to Eq. (7.22). On the other hand, Kaminski [30] made an experimental attempt to determine  $\tau_q$  in the hyperbolic heat equation, by measuring the time interval between when the heat source was turned on and when a temperature signal was detected. The heat source and the thermometer used were long needles, placed in parallel and separated by a gap of 5–20 mm. What the experiment actually measured was the average thermal diffusion speed  $v_{\text{dif}}$  if the cylindrical geometry and the initial conditions were properly taken into consideration in the analysis. The main problem with this frequently cited paper and similar studies in the 1990s was that most researchers did not realize that the hyperbolic heat equation is physically unjustified to be superior to the parabolic heat equation; instead, some researchers took the parabolic equation as a special case of the more general hyperbolic equation [3]. While many researchers have expressed doubt about the applicability of the hyperbolic heat equation, few have realized that an instantaneous response is merely a mathematical solution that does not affect the application of the diffusion equation in macroscopic problems. Electron gas and phonon gas in solids are quantum mechanical particles, which do not have memory of any kind. Ideal molecular gases obey classical statistics and do not have memory either, unless the deposited energy is too intense to cause ionization or reaction.

Does the temperature wave exist? What is a temperature wave anyway? In the early 1940s, Russian theoretical physicist Lev Landau (1908–1968) used a two-fluid model to study the behavior of quasiparticles in superfluid helium II and predicted the existence of a second sound, propagating at a speed between  $v_g/\sqrt{3}$  and  $v_g$ , depending on the temperature. Note that the group velocity is the same as the phase velocity for a linear dispersion. Above the  $\lambda$ -point, where superfluidity is lost, the second sound should also disappear. Landau was awarded the Nobel Prize in Physics in 1962 for his pioneering theories of condensed matter at low temperatures. He authored with his students a famous book series in mechanics and physics. Landau's prediction was validated experimentally by Russian physicists in the 1940s. The existence of a second sound in crystals was also postulated when scattering by defects becomes minimized. However, it was not until the mid-1960s that the second sound

associated with heat pulse propagation was observed in solid helium (below 1 K) and other crystals at low temperatures (below 20 K). The second sound can occur only at very low temperatures when the mean free path of phonons in the  $U$ -processes, in which the total momentum is not conserved, is longer than the specimen size; while at the same time, the scattering rate of the  $N$ -processes, in which the total momentum is conserved, is high enough to dominate other scattering processes. It should be noted that while the  $N$ -processes have a much shorter mean free path than the size of the specimen, scattering by  $N$ -processes does not dissipate heat (see Sect. 6.5.3). Callaway [31] simplified the BTE for phonon systems by a two-relaxation-time approximation, which should be applicable when  $t > \tau_N$ :

$$\frac{\partial f}{\partial t} + \mathbf{v} \cdot \frac{\partial f}{\partial \mathbf{r}} = \frac{f_0 - f}{\tau} + \frac{f_1 - f}{\tau_N} \quad (7.23)$$

where  $\tau$  stands for the relaxation time for the  $U$ -processes,  $\tau_N$  is the relaxation time for the  $N$ -processes, and  $f_0$  and  $f_1$  are the associated equilibrium distribution functions. Guyer and Krumhansl [32] solved the linearized BTE and derived the following equation for the phonon effective temperature:

$$\nabla^2 T + \frac{9\tau_N}{5} \frac{\partial}{\partial t} \nabla^2 T = \frac{3}{\tau v_a^2} \frac{\partial T}{\partial t} + \frac{3}{v_a^2} \frac{\partial^2 T}{\partial t^2} \quad (7.24)$$

where  $v_a$  is the average phonon speed. Assuming a linear dispersion, it can be evaluated using Eq. (5.10). Substituting  $\alpha = \tau v_a^2/3$ ,  $\tau_q = \tau$ , and  $\tau_T = 9\tau_N/5$ , we see that Eq. (7.24) is identical to Eq. (7.17). The condition  $t > \tau_N$  can be satisfied even at  $t < \tau$  since  $\tau_N \ll \tau$ . The significance of Eq. (7.24) lies in that the temperature wave or the second sound is not universal, but rather, requires strict conditions to be met [32]. When the condition  $\tau_N \ll \tau$  is satisfied, we have  $\tau_T \ll \tau_q$  and the energy transfer is dominated by wave propagation. At higher temperatures, the scattering rate for the  $U$ -processes is usually very high, and the  $N$ -processes contribute little to the heat conduction or thermal resistance, as discussed in Chap. 6. Therefore, the reason why temperature waves have not been observed in insulators at room temperature is not because of the small  $\tau$ , in the range from  $10^{-10}$  to  $10^{-13}$  s, but because of the lack of mechanisms required for a second sound to occur. No experiments have ever shown a second sound in metals, as suggested by the hyperbolic heat equation.

Shiomi and Maruyama [33] performed molecular dynamics simulations of the heat conduction through (5,5) single-walled carbon nanotubes, 25 nm in length, for several femtoseconds. They found that the wavelike behavior could be fitted by the lagging heat equation, but could not be described by the hyperbolic heat equation due to local diffusion. The ballistic nature of heat propagation in nanotubes has already been explained in Chap. 5. They suspected that optical phonons might play a major role in the non-Fourier conduction process [33]. Tsai and MacDonald [34] studied the strong anharmonic effects at high temperature and pressure using molecular dynamics. Their work predicted a second sound response. The coupling of elastic and thermal effects was thought to be important. Studies on thermomechanical

effects such as thermal expansion, thermoelasticity, and shock waves can be found from Tzou [6] and Wang and Xu [35, 36], and will not be discussed further.

Tang and Araki [26] clearly delineated four regimes in the lagging heat equation, according to the ratio  $\eta = \tau_r/\tau_q$ . (1) When  $\eta = 0$ , it is a damped wave, i.e., hyperbolic heat conduction. (2) When  $0 < \eta < 1$ , it is wavelike diffusion, for which wave features can be clearly seen if  $\eta \ll 1$ . (3) When  $\eta = 1$ , it is pure diffusion or diffusion, i.e., Fourier's conduction. (4) When  $\eta > 1$ , it is called over-diffusion, which makes the dimensionless temperature decay faster than pure diffusion would. In the next section, we will discuss a microscopic theory on short-pulse laser heating of metals, which falls in the regime of over-diffusion, or parallel conduction.

### 7.1.3 Two-Temperature Model

With a short laser pulse, 5 fs–500 ps, free electrons absorb radiation energy and the absorbed energy excites the electrons to higher energy levels. The “hot electrons” move around randomly and dissipate heat mainly through electron–phonon interactions. In the 1970s, Anisimov et al. [37] proposed a *two-temperature model*, which is a pair of coupled nonlinear equations governing the effective temperatures of electrons and phonons. This model was experimentally confirmed in the 1980s by researchers at the Massachusetts Institute of Technology [38, 39]. The two-temperature model was introduced to the heat transfer community by Qiu and Tien [40, 41] in early 1990s. In a series of papers [40–42], Qiu and Tien analyzed the size effect due to boundary scattering and performed experiments with thin metallic films. In the two-temperature model, it is assumed that the electron and phonon systems are each at their own local equilibrium, but not in mutual equilibrium. The electron temperature could be much higher than the lattice (or phonon) temperature due to absorption of pulse heating. Therefore,

$$C_e \frac{\partial T_e}{\partial t} = \nabla \cdot (\kappa \nabla T_e) - G(T_e - T_s) + \dot{q}_a \quad (7.25a)$$

$$C_s \frac{\partial T_s}{\partial t} = G(T_e - T_s) \quad (7.25b)$$

Here, the subscript e and s are for the electron and phonon systems, respectively,  $C$  is the volumetric heat capacity,  $G$  is the electron–phonon coupling constant, and  $\dot{q}_a$  is the source term that represents the absorbed energy rate per unit volume during the laser pulse and drops to zero after the pulse. Heat conduction by phonons is neglected, and thus, the subscript e is dropped in the thermal conductivity  $\kappa$ . Note that  $\mathbf{q}'' = -\kappa \nabla T_e$ , according to Fourier's law. We have already given a macroscopic example of parallel heat transfer, as shown in Fig. 7.3, which should ease the understanding of the phenomenological relations given in Eqs. (7.25a), (7.25b). Equations (7.25a), (7.25b) originate from microscopic interactions between photons, electrons, and phonons. In order to examine the parameters in Eqs. (7.25a), (7.25b) and their dependence

on  $T_e$  and  $T_s$ , let us assume that the lattice temperature is near or above the Debye temperature for simplicity. In such a case, electron–electron scattering and electron–defects scattering are insignificant compared with electron–phonon scattering. It is expected that the electron relaxation time is inversely proportional to the lattice temperature, i.e.,  $\tau \approx \tau_{e-ph} \propto T_s^{-1}$ . The meaning of the relaxation time is that the electron system can be assumed to be at internal local equilibrium when  $t > \tau$ , which is the condition for Eqs. (7.25a), (7.25b) to be applicable. Boundary scattering may play a role for very thin films or in polycrystalline materials. An effective mean free path can be introduced to modify the scattering rate [40, 43, 44]. The volumetric heat capacity for the lattice or phonons is  $C_s = \rho c_p$  is a weak function of the lattice temperature; the volumetric heat capacity of electrons, from Eq. (5.25), becomes

$$C_e = \frac{n_e \pi^2 k_B^2}{2\mu_F} T_e = \gamma T_e \quad (7.26)$$

Recall that  $C_e$  is relatively small compared with  $C_s$ , even at several thousand kelvins. From simple kinetic theory, the thermal conductivity is

$$\kappa = \frac{\pi^2 n_e k_B^2}{3m_e} \tau T_e \approx \frac{\kappa_{eq}}{T_s} T_e \quad (7.27)$$

where  $\kappa_{eq}$  is the thermal conductivity when  $T_e = T_s$ , which can be set at room temperature value. The term  $T_e$  in Eq. (7.27) comes from the heat capacity. The size effect can be included using an effective relaxation time. Theoretically, the coupling constant can be estimated by

$$G = \frac{\pi^2 m_e n_e v_a^2}{6\tau T_s} \text{ or } G = \frac{\pi^4 (n_e v_a k_B)^2}{18\kappa_{eq}} \quad (7.28)$$

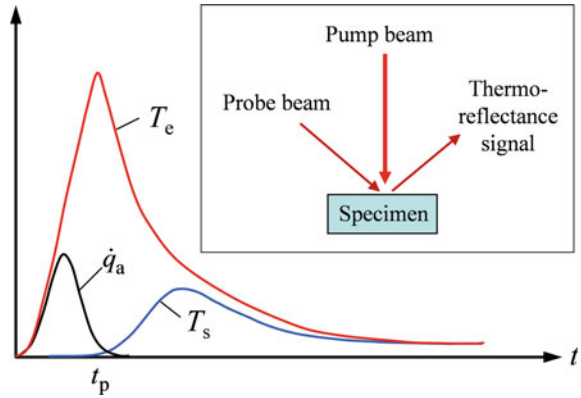
which is independent of temperature, when boundary scattering is not important, but proportional to the square of the speed of sound in the metal. With the speed of sound in the low-frequency limit, the dispersion is linear; thus, we do not have to worry about the difference between the phase velocity and the group velocity. From Eq. (5.10), we have

$$v_a = \frac{k_B \Theta_D}{h} \left( \frac{4\pi}{3n_a} \right)^{1/3} \quad (7.29)$$

When boundary scattering is included,  $G$  is expected to increase from the bulk value and depend on the lattice temperature. Using the Debye temperature and for  $n_a = n_e$ , we have

$$G = \frac{\pi^2}{12 \times \sqrt[3]{4}} \frac{n_e k_B^2 \Theta_D^2}{\tau T_s \mu_F} \approx 0.518 \frac{n_e k_B^2 \Theta_D^2}{\tau T_s \mu_F} \quad (7.30)$$

**Fig. 7.4** Illustration (not to scale) of ultrafast thermoreflectance experiments and the associated electron and phonon temperatures near the surface, during a short pulse



Typical values of  $G$  are on the order of  $10^{16}$  W/K m<sup>3</sup>, e.g.,  $G \approx 2.9 \times 10^{16}$  W/K m<sup>3</sup> for gold. The behavior of the electron and phonon temperatures near the surface is shown in Fig. 7.4, for a short pulse. The electron temperature rises quickly during the pulse and begins to decrease afterward; in the meantime, the lattice temperature gradually begins to increase until the electron and lattice systems reach a thermal equilibrium. Both the temperatures will go down as heat is carried away from the surface. Note that the electron temperature can rise very high due to its small heat capacity, but the lattice or solid may be just slightly above room temperature. If the temperatures of the electron and lattice were the same, Eqs. (7.25a), (7.25b) would reduce to the simple Fourier heat conduction equation. This would lead to a prediction of a much lower temperature rise, because the heat capacity of the lattice is much greater than that of the electrons.

Given such a short timescale and the nonequilibrium nature between electrons and phonons locally, no contact thermometer could possibly measure the effective electron temperature. Experiments are usually performed by the femtosecond or picosecond thermoreflectance technique, also known as the pump-and-probe method, shown in the inset of Fig. 7.4. The reflectance of the surface depends on the electron temperature  $T_e$ . The experimental setup is rather involved and the details will be given in Sect. 7.4.3. The procedure is to send a pump pulse train that is synchronized with a probe pulse train at a fixed delay time. The electron temperature change near the surface is related to the reflectance as a function of the delay time. Electron–phonon coupling, boundary scattering, and thermal boundary resistance can all affect the thermoreflectance signal. Comparing with the model described in Eqs. (7.25a), (7.25b), along with the dependence of the reflectance on the electron temperature, the microscopic characteristics can be analyzed. Ultrafast thermoreflectance techniques have become an important thermal metrology tool for the study of electron–phonon interactions, TBR, and thermophysical properties [40–49]. Thermionic emission can also occur from the surface, especially when the electrons are excited to higher energy states [50].

Similar to what has been done for Eqs. (7.21a) and (7.21b), Eqs. (7.25a) and (7.25b) can be combined to formulate partial differential equations for either the electron or phonon temperature. Neglecting the temperature dependence of the parameters, one obtains the following differential equations for the electron temperature and the phonon temperature, respectively,

$$\nabla^2 T_e + \tau_T \frac{\partial}{\partial t} \nabla^2 T_e + \frac{\dot{q}_a}{\kappa} + \frac{\tau_T}{\kappa} \frac{\partial \dot{q}_a}{\partial t} = \frac{1}{\alpha} \frac{\partial T_e}{\partial t} + \frac{\tau_q}{\alpha} \frac{\partial^2 T_e}{\partial t^2} \quad (7.31a)$$

$$\nabla^2 T_s + \tau_T \frac{\partial}{\partial t} \nabla^2 T_s + \frac{\dot{q}_a}{\kappa} = \frac{1}{\alpha} \frac{\partial T_s}{\partial t} + \frac{\tau_q}{\alpha} \frac{\partial^2 T_s}{\partial t^2} \quad (7.31b)$$

where  $\alpha = \frac{\kappa}{C_e + C_s}$ ,  $\tau_T = \frac{C_s}{G}$ , and  $\tau_q = \frac{\tau_T C_e}{C_e + C_s} \approx \frac{C_e}{G} \ll \tau_T$ . These equations are identical to the lagging heat equations and can be solved with appropriate boundary conditions. The results again belong to the regime of over-diffusion, or parallel conduction, without any wavelike features. Cooling caused by thermionic emission is usually neglected, and the surface under illumination can be assumed adiabatic. A 1D approximation further simplifies the problem. The solution follows the general trends depicted in Fig. 7.4. The situation will be completely changed if a phase change occurs or if the system is driven to exceed the linear harmonic behavior [6, 35].

The term  $\tau_q$  is clearly not the same as the relaxation time  $\tau$  due to collision. The resulting solution is more diffusive than wavelike. In the literature,  $\tau_q$  is commonly referred to as the *thermalization time*. The physical meaning of  $\tau_q$  is a *thermal time constant* for the electron system to reach an equilibrium with the phonon system. For noble metals at room temperature, the relaxation time  $\tau$  is on the order of 30–40 fs, the thermalization time  $\tau_q$  is 0.5–0.8 ps, and the *retardation time*  $\tau_T$  is 60–90 ps. In practice, we need to consider the temperature dependence of the parameters in Eqs. (7.25a, 7.25b), as mentioned earlier. Some numerical solutions, considering temperature dependence, and comparisons with experiments can be found from Smith et al. [51] and Tzou and Chiu [27]. Given that the two-temperature model cannot be applied to  $t < \tau$ , due to the limitation of Fourier's law, one may prefer to use a pulse width  $t_p$  between 100 and 200 fs and measure the response during several picoseconds until the thermalization process is complete, i.e., the electron and phonon temperatures become the same. This first-stage measurement allows the determination of the coupling constant  $G$ . In the case of a thin film, the TBR sets a barrier for heat conduction between the film and the substrate. The time constant of the film can range from several tens to hundreds of picoseconds. Therefore, the TBR between the film and the substrate can be determined by continuing the observation of thermoreflectance signals for 1–2 ns after each pulse. Fitting the curves in the second-stage measurement allows an estimate of the TBR. Of course, one could use a longer pulse width  $t_p$  to determine the TBR. Most advanced femtosecond research laboratories are equipped with Ti:sapphire lasers whose pulse widths range from 50 to 500 fs. Femtosecond lasers with a pulse width of 25 fs have also been used in some studies; see for example Li et al. [52]. For  $t_p$  below 50 fs, Eq. (7.25a) is not applicable during the heating, at least for noble metals. The relaxation time for Cr

is about 3 fs, and Eqs. (7.25a, 7.25b) can be safely applied even with  $t_p = 10$  fs. However, the processes below 20 fs may largely involve electron–electron inelastic scattering, thermionic emission, ionization, phase transformation, chemical reaction, and so forth. Other difficult issues associated with the reduced pulse width include widened frequency spectrum, increased pulse intensity, decreased pulse energy, and so forth. A simple hyperbolic formulation cannot properly address these issues. One must investigate the physical and chemical processes occurring at this timescale in order to develop a physically plausible model, with or without the concept of effective temperatures. Femtosecond laser interactions with dielectric materials have also been extensively studied (see Jiang and Tsai [53, 54] and references therein). Recently, Ma [55] proposed a two-parameter heat conduction model for analyzing transient heat conduction data for dielectric materials and for thermal interfaces based on both frequency-domain and time-domain measurements. In the two-parameter model, a nonequilibrium (effective) temperature is defined and used to obtain a nondiffusive phenomenological equation. A thermal conductivity (that describes diffusive thermal transport) and a ballistic heat transfer length (that is the product of a ballistic relaxation time and the speed of carriers) are taken as the fitting parameters [55]. It should be noted that the formulation of the two-parameter model differs significantly from the ballistic–diffusion heat conduction equations proposed by Chen [56] in 2001.

Let us reiterate some major points presented in this section: (a) Fourier’s law, which is limited to local-equilibrium conditions, does not predict an infinite speed of heat diffusion, nor does it violate the principle of causality [3]. An instantaneous response at a finite distance is permitted by quantum statistics although the probability of such a response sharply approaches zero as the distance increases. An instantaneous temperature change or heat flux at a precise location is not physically possible. Only under the continuum assumption, we can use the concept of sudden change of temperature at the boundary. (b) Heat diffusion is usually a very slow process, compared with the speed of sound. The temperature wave, or the second sound, has been observed only in helium and some very pure dielectric crystals, at low temperatures, where the  $U$ -processes are ballistic and the  $N$ -processes have a very high scattering rate. (c) Both Fourier’s law and Cattaneo’s equation can be derived from the BTE under slightly different approximations [17]. Fourier’s law is not an approximation of Cattaneo’s equation and, hence, Cattaneo’s equation is not more general than Fourier’s law. Nevertheless, the introduction of an additional parameter (the relaxation time) in Cattaneo’s equation may allow the hyperbolic heat equation to better fit some experiments in inhomogeneous medium with coupled phenomena [4]. (d) All kinds of non-Fourier equations are based on some sort of effective temperature, which are not measurable using a contact thermometer. The principle of contact thermometry is based on the assumption of thermodynamic equilibrium according to the zeroth law of thermodynamics. The concept of coldness or hotness should be abandoned in reference to nonequilibrium energy transport processes. Noncontact thermometry, on the other hand, relies on certain physical responses to deduce the equilibrium temperature or the effective temperature of the system being measured. (e) The memory hypothesis and the lagging argument are phenomenological models that may be useful in the study of certain nonequilibrium or parallel conduction

processes, but are not universally applicable. These and similar equations must be derived and applied on a case-by-case basis. It is important to understand the microscopic processes occurring at the appropriate length scales and timescales in order to develop physically reliable models.

## 7.2 Heat Conduction Across Layered Structures

In Sect. 5.5.2, we have given a detailed discussion on the heat conduction along a thin film using the BTE, under the local-equilibrium assumption. An effective thermal conductivity can be used after taking proper account of boundary scattering. The heat conduction problem can thus be well described by Fourier's law using the effective thermal conductivity. As mentioned earlier, for heat transfer across a film or a superlattice, the condition of local equilibrium breaks down in the acoustically thin limit. The local distribution function cannot be approximated by an equilibrium distribution function at any temperature. Conventional Fourier's law breaks down because it relies on the definition of an equilibrium temperature and the existence of local equilibrium. It is natural to ask the following two questions. (1) Is it possible for us to define an effective temperature? (2) Can Fourier's law still be useful in the nonequilibrium regime, according to the effective temperature? This section presents the equation of phonon radiative transfer (EPRT) and the solution of EPRT for thin films under the relaxation time approximation. A resistance network representation is used to illustrate how Fourier's law of heat conduction may be applied inside the medium, at least approximately, with temperature-jump boundary conditions. Because of the importance of understanding the boundary conditions, this section also discusses models of thermal boundary resistance (TBR) in layered structures.

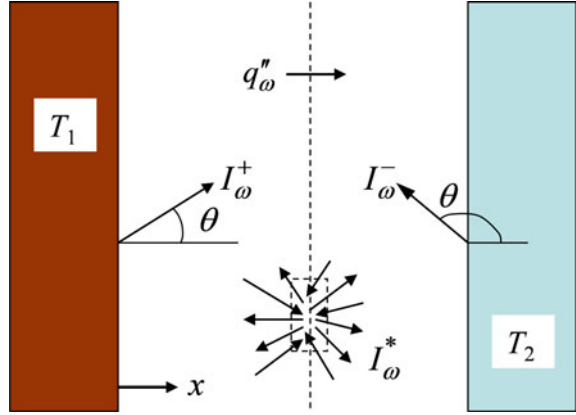
### 7.2.1 Equation of Phonon Radiative Transfer (EPRT)

The phonon BTE under the relaxation time approximation, in a region with heat generation, may be written as

$$\frac{\partial f}{\partial t} + \mathbf{v} \cdot \frac{\partial f}{\partial \mathbf{r}} = \frac{f - f_0}{\tau(\omega, T)} + S_0 \quad (7.32)$$

where the second term  $S_0$  on the right-hand side is a source term to model the generation of phonons due to heat dissipation, such as electron–phonon scattering. Phonon–phonon scattering is already included in the first term on the right-hand side. The scattering rate may also include phonon-defect scattering. Many studies have treated phonon transport in analogy to thermal radiative transfer [19, 20, 57–67]. In the following, a simplified case is used to illustrate how to model heat transfer across a thin film as well as multilayer structures. Let us consider a film of thickness

**Fig. 7.5** Schematic of phonon radiative transfer inside a dielectric medium between two walls maintained at temperatures  $T_1$  and  $T_2$ . These walls are like heat reservoirs, but their surfaces are not necessarily blackbodies



$L$  between two boundaries without any internal source. The phonon BTE becomes

$$\frac{\partial f}{\partial t} + v_x \frac{\partial f}{\partial x} = \frac{f_0 - f}{\tau} \quad (7.33)$$

Realizing the nonequilibrium distribution function may be anisotropic, let us define

$$I_\omega(x, \Omega, t) = \frac{1}{4\pi} \sum_P v_g \hbar \omega f D(\omega) \quad (7.34)$$

where  $P$  is the index for phonon mode or polarization and  $D(\omega)$  is the DOS. Equation (7.34) gives the *phonon intensity*, which is the energy transfer rate in the direction  $\Omega$  from a unit area, per unit frequency and per unit solid angle. The geometry of the problem and illustration of the intensity is given in Fig. 7.5. As done before, let  $v_g$  and  $v_p$  be the group velocity and phase velocity, respectively. Note that  $v_x = v_g \cos \theta$ , where  $\theta$  is the polar angle. Substituting Eq. (7.34) into Eq. (7.33), we obtain

$$\frac{1}{v_g} \frac{\partial I_\omega}{\partial t} + \mu \frac{\partial I_\omega}{\partial x} = \frac{I_\omega^* - I_\omega}{v_g \tau} \quad (7.35)$$

where  $\mu = \cos \theta$  and  $I_\omega^*(\omega, T)$  is the intensity for equilibrium distribution that is independent of the direction. Equation (7.35) is called the equation of phonon radiative transfer (EPRT) [19, 61]. Comparing the EPRT with the ERT given in Eq. (2.53), we see that the scattering terms are neglected in the EPRT, and the emission and absorption are replaced by the phonon collision terms. The phonon mean free path  $\Lambda = v_g \tau$  is also called the phonon penetration depth (see Example 4.2). The inverse of the penetration depth ( $1/\Lambda$ ) corresponds to the absorption coefficient in the ERT. Conversion to the EPRT allows well-established theories and numerical techniques, developed in radiative transfer, to be applied to solve Eq. (7.35) and to interpret the

physical significance of the solutions [68, 69]. If  $\tau$  does not depend on frequency, we are dealing with a gray medium.

If the phonon Knudsen number  $Kn = \Lambda/L \ll 1$ , then most phonons will collide with phonons or defects inside the medium. This regime is called the *acoustically thick limit*, in analogy to the *optically thick limit* for photons. This is also known as the macroscale regime or the local-equilibrium situation. Unless at a very short timescale, when a sudden local disturbance occurs, we expect that Fourier's law is applicable and the heat conduction is by diffusion. On the other hand, if  $Kn = \Lambda/L \gg 1$ , phonons originated from one boundary will most likely reach the other boundary without colliding with other phonons or defects inside the medium. This is the ballistic regime, corresponding to free molecule flow for molecular gases. This regime is called the *acoustically thin limit*, where the phonon distribution inside the medium cannot be characterized by an equilibrium distribution function if the walls are at different temperatures, even in the steady state. Because the BTE is more fundamental than Fourier's law, it is applicable to both limiting cases as well as those between the two limits. It would be very useful if a macroscopic model can also be developed to bridge these two limits. Some basic formulations are given in the following.

Note that  $I_\omega^*$  is the equilibrium distribution function, which is independent of the direction. Using Bose–Einstein statistics, we have

$$I_\omega^*(\omega, T) = \sum_P \frac{v_g \hbar \omega}{e^{\hbar \omega / k_B T} - 1} \frac{k^2}{(2\pi)^3} \frac{dk}{d\omega} = \sum_P \frac{\hbar \omega^3}{8\pi^3 v_p^2 (e^{\hbar \omega / k_B T} - 1)} \quad (7.36)$$

This equilibrium distribution is also the distribution function for blackbody radiation with  $v_p$  replaced by the speed of light. Integrating Eq. (7.36) over all frequencies gives the total intensity for all three phonon modes:

$$I^*(T) = \int_0^\infty I_\omega^*(\omega, T) d\omega = \frac{3k_B^4 T^4}{8\pi^3 \hbar^3 v_a^2} \int_0^\infty \frac{x^3 dx}{e^x - 1} = \frac{\sigma'_{SB} T^4}{\pi} \quad (7.37)$$

where  $\sigma'_{SB} = \pi^2 k_B^4 / (40 \hbar^3 v_a^2)$  is the phonon Stefan–Boltzmann constant, and  $v_a$  is the average phase velocity of the two translational and one longitudinal phonon modes, defined according to Eq. (5.7). Let us consider a solid at temperatures higher than the Debye temperature. The integration can be carried out to an upper limit  $\omega_m$  with  $x_m = \hbar \omega_m / (k_B T) \ll 1$ . From the discussion following Eq. (5.13), one can easily show that

$$I^*(T) = \int_0^{\omega_m} I_\omega^*(\omega, T) d\omega = \frac{\omega_m^3 k_B}{8\pi^3 v_p^2} T \quad (7.38)$$

This integration is a good approximation, even at temperatures slightly lower than the Debye temperature. When phonons are at equilibrium, the energy flux is

$\pi I^*$ , which is obtained by integrating  $I^* \cos\theta \, d\Omega$  over the hemisphere. According to Eq. (4.12), the energy density can be expressed as

$$u(T) = \frac{4\pi}{v_g} I^*(T) \quad (7.39)$$

Note that the volumetric heat capacity  $C = du/dT$  when  $u$  is expressed in terms of energy density. We therefore obtain the low-temperature relation of the specific heat, i.e., the  $T^3$  law, and the high-temperature relation of the specific heat, i.e., the Dulong–Petit law, as already derived in Sect. 5.1.2. It is important to pay attention to the meaning of  $C$  in the kinetic expression of thermal conductivity:

$$\kappa = \frac{1}{3} C v_g^2 \tau \quad (7.40)$$

At very low temperatures, when  $T \ll \Theta_D$ ,  $C$  is the volumetric heat capacity of all phonon modes combined because only low-frequency modes or acoustic branches contribute to the specific heat. However, at temperatures close to the Debye temperature, phonons in the optical branches contribute little to the thermal conductivity, as already discussed in Chap. 6. The relative contributions of LA and TA branches are also temperature dependent. The Debye temperature for most materials, except diamond, is not much higher than room temperature (see Table 5.1). Therefore, one may treat the volumetric heat capacity  $C$  as a fraction of the volumetric specific heat in dealing with Si, GaAs, Ge, ZnS, or GaN, near room temperature. Also, we must use the appropriate upper limit in the integral in calculating the total energy transfer when applying EPRT. The heat flux per unit frequency interval can thus be expressed as

$$q''_{\omega} = \int_{4\pi} I_{\omega} \cos\theta \, d\Omega = 2\pi \int_{-1}^1 I_{\omega} \mu \, d\mu \quad (7.41)$$

Energy balance at any given location requires that the incoming flux from all directions be the same as the outgoing flux toward all directions, for both steady and transient states, as illustrated in Fig. 7.5. This is the criterion for *radiative equilibrium* [68, 69], which can be expressed as follows [19]:

$$4\pi \int_0^{\omega_m} \frac{1}{\Lambda_{\omega}} I_{\omega}^* \, d\omega = 2\pi \int_0^{\omega_m} \int_{-1}^1 \frac{1}{\Lambda_{\omega}} I_{\omega} \, d\mu \, d\omega \quad (7.42)$$

where  $\Lambda_{\omega}$  is the mean free path at  $\omega$ ,  $4\pi$  on the left-hand side came from the integration over all solid angles in a sphere, and  $2\pi$  on the right-hand side came from integration over the azimuth angles. For a gray medium,  $\Lambda_{\omega} = v_a \tau$  is independent of the frequency. Equation (7.42) gives a definition of an *effective phonon temperature*

$T^*$  based on the equilibrium distribution:  $I_\omega^*(T^*, \omega)$ . An equivalent expression can be obtained based on the energy density, viz.

$$u(T^*) - u_0 = \sum_P \sum_K \hbar \omega f_0(T^*, \omega, \Omega) = \sum_P \sum_K \hbar \omega f(\omega, \Omega) \quad (7.43)$$

where  $u_0$  is a reference value. Note that the spectral component (integrand) on both sides of Eq. (7.42) may not be equal at all frequencies. Even for a gray medium, in general, one cannot deduce the following from Eq. (7.42):

$$I_\omega^*(T^*, \omega) = \frac{1}{2} \int_{-1}^1 I_\omega d\mu \quad (7.44)$$

The physical significance of Eq. (7.44) is that the angular average of the intensity, at a given location and time, can be described by an equilibrium intensity that satisfies the equilibrium distribution function at a certain temperature. As a matter of fact, Eq. (7.44) is equivalent to the *local-equilibrium approximation* [70]. It can be shown that the local-equilibrium approximation is valid only in the acoustically thick limit or the diffusive heat conduction regime.

**Example 7.3** For a dielectric medium of thickness  $L = 0.01\Lambda$ , the mean free path  $\Lambda$  is independent of wavelength. The boundary or wall temperatures are  $T_1 = 50$  K at  $x = 0$  and  $T_2 = 100$  K at  $x = L$ . Both the temperatures are much lower than the Debye temperature. Assume that reflection at the boundaries is negligible, i.e., the walls can be modeled as blackbodies. At steady state, express the heat flux through the medium and find the effective photon temperature distribution  $T^*(x)$ .

**Solution** Because  $Kn = \Lambda/L \gg 1$ , the medium is said to be in the acoustically thin limit, in which phonons travel from one wall to another ballistically with little chance of being scattered by other phonons or defects inside the medium. The forward intensity can be expressed as  $I_\omega^+ = I_\omega^*(T_1, \omega)$  for  $\mu > 0$ , and the backward intensity  $I_\omega^- = I_\omega^*(T_2, \omega)$  for  $\mu < 0$ . From Eq. (7.41), we have

$$q_x'' = \int_0^\infty q_\omega'' d\omega = 2\pi \int_0^\infty \int_0^1 (I_\omega^+ - I_\omega^-) \mu d\mu d\omega = \sigma'_{\text{SB}} (T_1^4 - T_2^4) \quad (7.45)$$

For heat conduction, the above equation is called the Casimir limit [71]. To numerically evaluate this equation, we need data for  $\nu_a$ . From Eq. (7.42), we have

$$\sigma'_{\text{SB}} (T^*)^4 = \frac{\pi}{2} \int_0^{\omega_n} (I_\omega^+ + I_\omega^-) d\omega = \frac{1}{2} (\sigma'_{\text{SB}} T_1^4 + \sigma'_{\text{SB}} T_2^4) \quad (7.46)$$

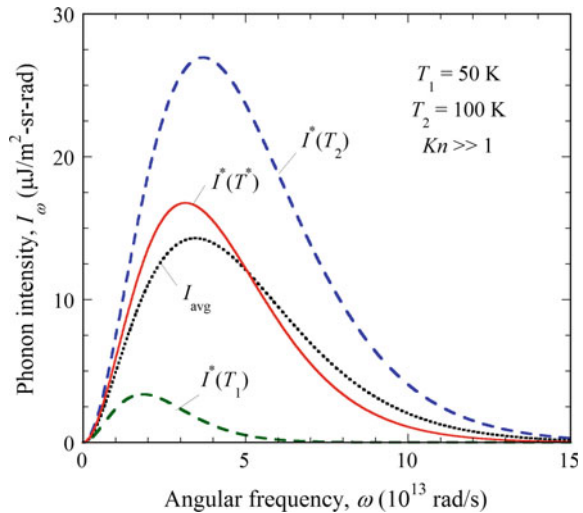
We obtain  $T^* = 85.37$  K, which is the effective temperature inside the medium  $0 < x < L$  and is independent of  $x$ . Since  $T(0) = T_1$  and  $T(L) = T_2$  are the boundary conditions, there is a temperature jump at each boundary similar to Fig. 4.12b in the free molecule regime for gas conduction. If the walls are not black but diffuse-gray with emissivities  $\varepsilon_1$  and  $\varepsilon_2$ , similar to Eq. (2.52), the heat flux becomes

$$q_x'' = \frac{\sigma'_{SB} T_1^4 - \sigma'_{SB} T_2^4}{1/\varepsilon_1 + 1/\varepsilon_2 - 1} \quad (7.47)$$

**Comments:** (1) Taking diamond with  $v_a = 12,288$  m/s as an example, we have  $\sigma'_{SB} = 50.63$  W/m<sup>2</sup> K<sup>4</sup>. The magnitude of the heat flux in the ballistic limit for  $T_1 = 50$  K and  $T_2 = 100$  K is 4.75 GW/m<sup>2</sup>, which is quite high. Note that the mean free path of diamond in this temperature region is around 1.3  $\mu$ m [19, 70]. Thus when  $Kn = 100$ , the thickness is only 13 nm. If an effective diffusive thermal conductivity is used,  $\kappa_{\text{eff}} = 1.23$  W/m K, which is much smaller than the bulk thermal conductivity of diamond! In general, ballistic transport in nanostructures results in a restriction to the heat flow as compared with diffuse transport with the same thermal conductivity. (2) Figure 7.6 shows the phonon intensity spectra at  $T_1$ ,  $T_2$ , and  $T^*$  for diamond, calculated from Eq. (7.36) for the sum of the three phonon modes taking the average velocity  $v_a$  in place of  $v_p$ . We notice immediately that Eq. (7.44) cannot be satisfied in the acoustically thin limit. Let us designate

$$I_{\text{avg}}(\omega) = \frac{1}{2} \int_{-1}^1 I_\omega d\mu = \frac{1}{2} (I_\omega^+ + I_\omega^-) \quad (7.48)$$

**Fig. 7.6** Phonon intensity spectra for equilibrium distribution at the wall temperatures  $T_1$  and  $T_2$ , and the effective temperature  $T^*$ . The intensity calculated based on Eq. (7.48) is also plotted for comparison. Note that  $I_{\text{avg}}(\omega)$  may be considered as a nonequilibrium distribution in terms of the phonon intensity



which is also plotted in Fig. 7.6. It can be seen that  $I_{\omega}^*(\omega) \neq I_{\text{avg}}(\omega)$  in general. It is well known that a monochromatic temperature can be defined and is useful in radiation thermometry (refer to Sect. 8.2 for further discussion). Bright and Zhang [70] used the concept of monochromatic phonon temperature to study entropy generation in a thin film from the diffusive regime to the ballistic regime.

### 7.2.2 Solution of the EPRT

The two-flux method is very helpful in developing a solution of the EPRT in planar structures, as shown in Fig. 7.5. The equations for the forward and backward intensities, denoted respectively by superscripts (+) and (-), can be separated. Assuming the medium is gray, at steady state, we can rewrite the EPRT given in Eq. (7.35) as follows [68, 69]:

$$\mu \frac{\partial I_{\omega}^+}{\partial x} = \frac{I_{\omega}^* - I_{\omega}^+}{\Lambda}, \text{ when } 0 < \mu < 1 \quad (7.49a)$$

$$\mu \frac{\partial I_{\omega}^-}{\partial x} = \frac{I_{\omega}^* - I_{\omega}^-}{\Lambda}, \text{ when } -1 < \mu < 0 \quad (7.49b)$$

If we further assume that the walls are diffuse and gray, then the boundary conditions become

$$T(0) = T_1 \text{ and } T(L) = T_2 \quad (7.50)$$

Thus,

$$I_{\omega}^+(0, \mu) = \varepsilon_1 I_{\omega}^*(T_1) + (1 - \varepsilon_1) I_{\omega}^-(0, \mu) \quad (7.51a)$$

$$I_{\omega}^-(L, \mu) = \varepsilon_2 I_{\omega}^*(T_2) + (1 - \varepsilon_2) I_{\omega}^+(L, \mu) \quad (7.51b)$$

The solutions of Eqs. (7.49a) and (7.49b) can be expressed as follows:

$$I_{\omega}^+(x, \mu) = I_{\omega}^+(0, \mu) \exp\left(-\frac{x}{\Lambda\mu}\right) + \int_0^x I_{\omega}^*(\xi) \exp\left(-\frac{x-\xi}{\Lambda\mu}\right) \frac{d\xi}{\Lambda\mu} \text{ for } \mu > 0 \quad (7.52a)$$

and

$$I_{\omega}^-(x, \mu) = I_{\omega}^-(L, \mu) \exp\left(\frac{L-x}{\Lambda\mu}\right) - \int_x^L I_{\omega}^*(\xi) \exp\left(-\frac{x-\xi}{\Lambda\mu}\right) \frac{d\xi}{\Lambda\mu} \text{ for } \mu < 0 \quad (7.52b)$$

In Eq. (7.53), the first term represents intensity originated from the left surface, after being attenuated, and the second term is the contribution of generation that is subject to attenuation as well. Equation (7.54) is viewed reversely for intensity from the right to the left. The spectral heat flux, defined in Eq. (7.41), can be obtained

$$q''_{\omega} = 2\pi \int_0^1 \left[ I_{\omega}^{+}(0, \mu) \exp\left(-\frac{x}{\Lambda\mu}\right) - I_{\omega}^{-}(L, -\mu) \exp\left(-\frac{L-x}{\Lambda\mu}\right) \right] \mu d\mu \\ + 2\pi \int_0^x I_{\omega}^{*}(\xi) E_2\left(\frac{x-\xi}{\Lambda}\right) \frac{d\xi}{\Lambda} - 2\pi \int_x^L I_{\omega}^{*}(\xi) E_2\left(\frac{\xi-x}{\Lambda}\right) \frac{d\xi}{\Lambda} \quad (7.53)$$

where  $E_m(x) = \int_0^1 \eta^{m-2} e^{-x/\eta} d\eta$  is again the  $m$ th-order *exponential integral*. If the surface is diffuse, then we have

$$q''_{\omega} = 2\pi I_{\omega}^{+}(0) E_3\left(\frac{x}{\Lambda}\right) - 2\pi I_{\omega}^{-}(L) E_3\left(\frac{L-x}{\Lambda}\right) \\ + 2\pi \int_0^x I_{\omega}^{*}(\xi) E_2\left(\frac{x-\xi}{\Lambda}\right) \frac{d\xi}{\Lambda} - 2\pi \int_x^L I_{\omega}^{*}(\xi) E_2\left(\frac{\xi-x}{\Lambda}\right) \frac{d\xi}{\Lambda} \quad (7.54)$$

Energy balance requires that the derivative of the radiative heat flux be zero, viz.

$$\frac{dq''_x}{dx} = \int_0^{\omega_m} \frac{\partial}{\partial x} q''_{\omega}(x, \omega) d\omega = 0 \quad (7.55)$$

This equation is another form of radiative equilibrium since radiative equilibrium means that the divergence of the radiative heat flux to be zero or  $\nabla \cdot \mathbf{q}'' = 0$ . Differentiating Eq. (7.54) yields

$$\frac{\partial q''_{\omega}}{\partial x} = -\frac{2\pi}{\Lambda} I_{\omega}^{+}(0) E_2\left(\frac{x}{\Lambda}\right) - \frac{2\pi}{\Lambda} I_{\omega}^{-}(L) E_2\left(\frac{L-x}{\Lambda}\right) \\ - \frac{2\pi}{\Lambda} \int_0^L I_{\omega}^{*}(\xi) E_1\left(\frac{|x-\xi|}{\Lambda}\right) \frac{d\xi}{\Lambda} + \frac{4\pi}{\Lambda} I_{\omega}^{*}(x) \quad (7.56)$$

In radiative transfer, we call  $J_1 = \int \pi I_{\omega}^{+}(0) d\omega$  and  $J_2 = \int \pi I_{\omega}^{-}(L) d\omega$  the total radiosities at surfaces 1 and 2, respectively, and  $e_b(T) = \int \pi I_{\omega}^{*} d\omega$  the total black-body emissive power. Substituting Eq. (7.56) into Eq. (7.55), after performing the integration, we obtain

$$2e_b(T(x)) = J_1 E_2\left(\frac{x}{\Lambda}\right) + J_2 E_2\left(\frac{L-x}{\Lambda}\right) + \int_0^L e_b(T(\xi)) E_1\left(\frac{|x-\xi|}{\Lambda}\right) \frac{d\xi}{\Lambda} \quad (7.57)$$

This is the radiative equilibrium condition and it is always valid if there is no internal generation. Note that Eq. (7.56) becomes zero for all frequencies only in the diffusive limit.

**Example 7.4** Find the temperature distribution, heat flux, and thermal conductivity for a gray medium with diffuse-gray surfaces in the acoustically thick limit, i.e.,  $Kn \ll 1$ ; under two extreme conditions: (i)  $T_1, T_2 \ll \Theta_D$  and (ii)  $T_1, T_2 > \Theta_D$ .

**Solution** In the thick limit, the first two terms in Eq. (7.53) can be dropped as long as  $x$  is not too close to either surface. Applying the first-order Taylor expansion  $I_\omega^*(x) = I_\omega^*(\xi) + \frac{dI_\omega^*}{dx}(x-\xi) + \dots$  and letting  $z = \frac{x-\xi}{\Lambda}$  in the third and fourth terms, we obtain

$$q_\omega'' = -4\pi\Lambda \frac{\partial I_\omega^*}{\partial x} \int_0^\infty z E_2(z) dz = -\frac{4\pi}{3} \Lambda \frac{\partial I_\omega^*}{\partial x} \quad (7.58)$$

Since  $\int_0^\infty z E_2(z) dz = 1/3$ . In fact, this equation applies to everywhere inside the medium because the spectral heat flux is continuous in the acoustically thick limit. Integrating Eq. (7.58) over the frequencies of interest, we see that under condition (i):

$$q_x'' = -\frac{16\sigma'_{SB} T^3}{3} \Lambda \frac{dT}{dx}, \text{ when } T \ll \Theta_D \quad (7.59)$$

This is nothing but a heat diffusion equation if we define the thermal conductivity as

$$\kappa(T) = \frac{16}{3} \sigma'_{SB} T^3 \Lambda \quad (7.60)$$

Comparing Eq. (7.60) with Eq. (7.40),  $\kappa(T) = \frac{1}{3} C v_g \Lambda$ , we see that  $C v_g = 16\sigma'_{SB} T^3$  in this case and it is consistent with the  $T^3$  law for the specific heat at low temperatures. In the thick limit, the temperature distribution is continuous at the wall, i.e.,  $T(0^+) = T(0) = T_1$  and  $T(L^-) = T(L) = T_2$ . Furthermore, the radiosity at the wall becomes the blackbody emissive power, even though the surface is not black. Hence, we can integrate Eq. (7.59):

$$\int_0^L q_x'' dx = \frac{4\Lambda}{3} \sigma'_{SB} \int_{T_1}^{T_2} 4T^3 dT \quad (7.61a)$$

which gives

$$q_x'' = \frac{4}{3}Kn(\sigma_{\text{SB}}'T_1^4 - \sigma_{\text{SB}}'T_2^4) \quad (7.61b)$$

as well as the temperature distribution:

$$T(x) = \left[ T_1^4 - \frac{x}{L}(T_1^4 - T_2^4) \right]^{1/4} \quad (7.62)$$

This distribution is linear in terms of the fourth power of temperature [69, 70]. From the definition of thermal resistance  $q_x'' = (T_1 - T_2)/R_t'$ , we have

$$R_t'' = \frac{3(T_1 + T_2)(T_1^2 + T_2^2)}{4\sigma_{\text{SB}}'Kn} \quad (7.63)$$

Under condition (ii), when the temperature is greater than the Debye temperature, we have

$$q_x'' = -\frac{\omega_m^3 k_B}{6\pi^2 v_p^2} \Lambda \frac{dT}{dx} \text{ when } T > \Theta_D \quad (7.64)$$

Compared with Eq. (7.40), we obtain

$$Cv_g = \frac{\omega_m^3 k_B}{2\pi^2 v_p^2} \quad (7.65)$$

This suggests that the specific heat is independent of temperature in the high-temperature limit as expected. A proper  $\omega_m$  should be chosen so that only propagating phonons or acoustic phonons are considered [61]. Assuming that the temperature difference is small so that we can approximate the thermal conductivity as a constant, we have

$$q_x'' = \frac{1}{3}Cv_g Kn(T_1 - T_2) \quad (7.66)$$

The thermal resistance becomes  $R_t'' = 3/(Cv_g Kn)$ , which increases as  $L$  increases. The temperature distribution is linear. One should realize that the scattering rate increases with temperature and depends on the frequency, due to phonon-phonon scattering. If we look at the radiative equilibrium condition again, by assuming  $T_1 > T_2$ , we see that  $I_\omega^+ > I_\omega^* > I_\omega^-$ . Therefore, local equilibrium is not a stable-equilibrium state. In the thick limit, the difference between  $I_\omega^+$  and  $I_\omega^-$  is caused by the spatial variation of  $I_\omega^*$  as can be clearly seen from Eqs. (7.52a) and (7.52b). Hence, the local-equilibrium approximation given in Eq. (7.44) is valid.

**Comment.** In the acoustically thin limit under the condition (ii) that  $T > \Theta_D$ , by using the linear temperature relationship given in Eq. (7.38), we can modify Eq. (7.45) to the following,

$$q_x'' = \frac{1}{4} C v_g (T_1 - T_2) \quad (7.67)$$

Here, we have used the definition of Eq. (7.65). The effective thermal conductivity in the ballistic limit:  $\kappa_{\text{eff}} = 3\kappa_b/(4Kn)$ , where  $\kappa_b$  is the bulk or diffusive thermal conductivity. It can be seen that in the ballistic regime, the thermal conductivity is inversely proportional to  $Kn$ .

Although no closed form exists for the solution of the ERT between the thick and thin limits, a number of approximation techniques and numerical methods can be used to provide satisfactory solutions, such as the discrete ordinates method ( $S_N$  approximation) and the spherical harmonics method ( $P_N$  approximation) [69]. It is important to see that, except in the thick limit, energy transfer occurs inside the medium in two ways: one is through exchange with the walls, and the other is through diffusion. For this reason, a ballistic-diffusion approximation has been developed to solve the EPRT [56]. In general, the temperature distribution looks like that in Fig. 4.12b if  $T_2$  is comparable to the Debye temperature. If  $T_1 \ll \Theta_D$ , then the temperature distribution can be plotted in terms of  $T^4$  so that the distribution looks more or less linear. There exists a temperature jump such that  $T(0^+) \neq T(0)$  and  $T(L^-) \neq T(L)$ , except in the thick limit. Understanding that the temperature is only an effective temperature and given such a temperature distribution, one may assume that there is a thermal resistance at each boundary and an internal thermal resistance, which may be described by Fourier's heat conduction [64]. For thermal radiative transfer in the absence of heat conduction, there exists a radiation slip or radiation jump at the boundary, unless the medium is optically thick. Without a participating medium, photons do not scatter on itself to dissipate heat or transfer heat by diffusion. This is a distinction between photons and phonons. Radiation slip is manifested by a discontinuous change of the intensity at the boundary. The temperature in the medium adjacent to the wall differs from the surface temperature. Such a temperature jump does not exist in classical Fourier's heat conduction theory; however, both velocity slip and temperature jump have already been incorporated in microfluidics research, as discussed in Chap. 4; see Eq. (4.99). The temperature-jump concept was first applied in the study of heat conduction in rarefied gases over 100 years ago. A straightforward approach for phonon transport is to sum up the thermal resistances in the acoustically thin and thick limits. The heat flux at very low temperatures can be expressed as

$$q_x'' = \frac{4\Lambda}{3L} \frac{\sigma'_{\text{SB}}(T_1^4 - T_2^4)}{1 + \left(\frac{1}{\varepsilon_1} - \frac{1}{2} + \frac{1}{\varepsilon_2} - \frac{1}{2}\right) \frac{4Kn}{3}} \quad (7.68)$$

Here, we separately write  $\left(\frac{1}{\varepsilon_1} - \frac{1}{2}\right)$  and  $\left(\frac{1}{\varepsilon_2} - \frac{1}{2}\right)$  to emphasize the thermal resistance due to radiation slip at each boundary. In the thick limit, the temperature jump approaches zero as  $Kn \rightarrow 0$ . Basically, Eq. (7.68) reduces to Eqs. (7.47) and (7.61b), in the extreme cases. If the walls can be treated as blackbodies with  $\varepsilon_1 = \varepsilon_2 = 1$ , and the temperature difference between  $T_1$  and  $T_2$  is small, we can approximate the heat flux as follows:

$$q_x'' = \frac{\kappa_b}{L} \frac{\Delta T}{1 + 4Kn/3} = \kappa_{\text{eff}} \frac{\Delta T}{L} \quad (7.69)$$

where  $\Delta T = T_1 - T_2 \ll T_2 < T_1$ , the bulk thermal conductivity  $\kappa_b(T) = \frac{16}{3}\sigma_{\text{SB}}' T^3 \Lambda$ , and the effective conductivity of the film is

$$\kappa_{\text{eff}} = \frac{\kappa_b}{1 + 4Kn/3} \quad (7.70)$$

At relatively high temperatures close to the Debye temperature, from Eqs. (7.66) and (7.67), we can write

$$q_x'' = \frac{\kappa_b}{L} \frac{T_1 - T_2}{1 + \left(\frac{1}{\varepsilon_1} + \frac{1}{\varepsilon_2} - 1\right) \frac{4Kn}{3}} = \kappa_{\text{eff}} \frac{T_1 - T_2}{L} \quad (7.71)$$

where  $\kappa_b(T) = \frac{1}{3}Cv_g\Lambda$ . Equation (7.71) gives the same conductivity ratio  $\kappa_{\text{eff}}/\kappa_b$  as in Eq. (7.70) for blackbody walls. These effective thermal conductivities are on the same order of magnitude as we have derived in Sect. 5.5.5, based on simple geometric arguments and Matthiessen's rule for the mean free path given in Eq. (5.128). In previous chapters, however, we did not elaborate in detail on the nature of nonequilibrium and the necessity of defining an effective temperature. It is interesting that different schools of thought can result in rather consistent results. The heat diffusion equation per se cannot tell us the cause of a temperature jump or how to evaluate it. The phonon BTE enables us to explore the microscopic phenomena and helps to evaluate the parameters and the properties. The microscopic understanding and the macroscopic phenomenological equations can work together to provide an effective thermal analysis tool.

The results presented previously are consistent with the detailed derivation of the temperature jump or the radiation slip, originally formulated by Deissler [72], for thermal radiation in gases not too far from the optically thick limit. Nevertheless, the expressions given here can be approximately applied between the diffusion and ballistic extremes [70]. It should be noted that when the temperature jump is treated as a thermal resistance at the boundary, Fourier's law can be used for the heat conduction inside the medium with bulk thermal conductivity. This is very different from heat conduction along the film.

While the meaning of emissivity for optical radiation is very clear, a question still remains as how to interpret the boundary conditions in the case of phonon conduction,

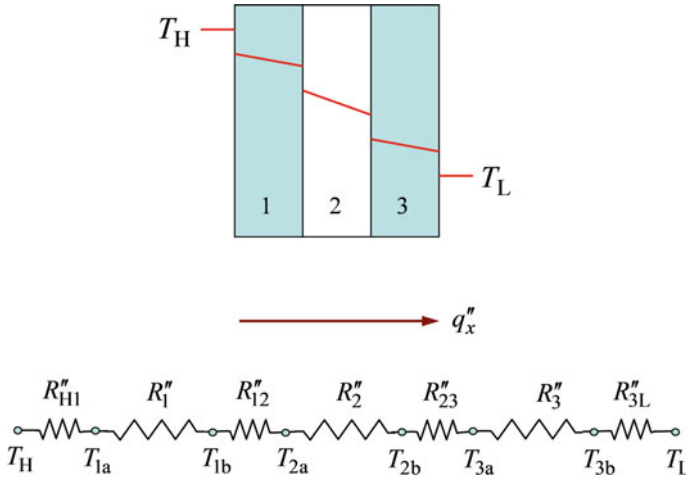


**Fig. 7.7** Temperature distribution in a multilayer structure, with thermal boundary resistance, and the thermal resistance network representation. Here,  $R_i''$  is the internal resistance in the  $i$ th layer due to heat conduction, and  $R_{ij}''$  is the thermal boundary resistance between the  $i$ th and  $j$ th media. Two temperatures are needed to specify the effective temperature of different media at the interface

since it is not easy to perceive the concepts of phonon emission and emissivity. If a multilayer structure is considered, we need to better understand the reflection and the transmission of phonons at the interfaces between dissimilar materials. A three-layer structure is shown in Fig. 7.7 to illustrate the temperature distribution in a multilayer structure. Depending on the temperature range, we may express the internal thermal resistance using Fourier’s law, i.e.,  $R_i'' = L_i/\kappa_i$ , where  $\kappa_i$  is the effective thermal conductivity of the  $i$ th layer. For the thermal resistance at the interface inside the layered structures, we could replace the emissivity with a transmissivity  $\Gamma_{ij}$  such that [64]

$$R_{ij}'' = \frac{4\Lambda_i}{3\kappa_i} \left( \frac{1}{\Gamma_{ij}} - \frac{1}{2} \right) + \frac{4\Lambda_j}{3\kappa_j} \left( \frac{1}{\Gamma_{ji}} - \frac{1}{2} \right) \tag{7.72}$$

At the boundaries, we can still use  $R_{H1}'' = \frac{4\Lambda_1}{3\kappa_1} \left( \frac{1}{\epsilon_1} - \frac{1}{2} \right)$  and  $R_{3L}'' = \frac{4\Lambda_3}{3\kappa_3} \left( \frac{1}{\epsilon_3} - \frac{1}{2} \right)$ .

The heat flux can be estimated by  $q_x'' = (T_H - T_L)/R_{tot}''$ , where  $R_{tot}''$  is the sum of all thermal resistances. The effective thermal conductivity of the whole layered structure becomes  $\kappa_{eff} = L_{tot}/R_{tot}''$ . The details were presented by Chen and Zeng [64], who further considered nondiffuse surfaces and defined equivalent equilibrium temperatures. The assumption is that the deviation from the thick limit is not significant. If we are dealing with the ballistic regime, we might need to consider phonon wave effects as well as the quantum size effect. Recently, Maldovan’s group has performed comprehensive studies of phonon transport across superlattices considering surface roughness and various length scales [73, 74]. The thermal resistance network

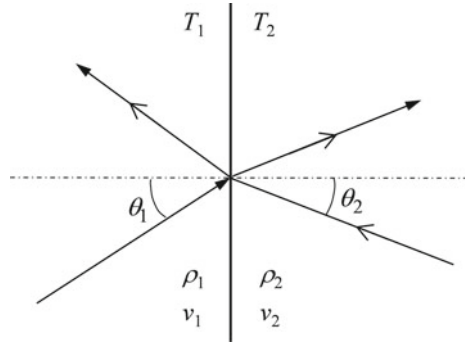
method, however, cannot be easily extended to multidimensional problems or to transient heating by a localized heat source. Statistical models (such as the Monte Carlo method) or atomistic simulations (such as the atomistic Green's function method or molecular dynamics) are necessary. Therefore, the extension of Fourier's law for 1D nonequilibrium heat transfer should be considered only as a special case. It is intriguing to apply the same approach to electron systems for the study of both electrical conductivity and thermal conductivity of metallic solids, as well as metal-dielectric multilayer structures. Further discussion on the classical and advanced models of thermal boundary resistance is given in the next section.

### 7.2.3 Thermal Boundary Resistance (TBR)

Thermal resistance at the interface between dissimilar materials is very important for heat transfer in heterostructures. Let us first clarify the difference between thermal contact resistance and thermal boundary resistance (TBR). The former refers to the thermal resistance between two bodies, usually with very rough surfaces whose root-mean-square roughness  $\sigma_{\text{rms}}$  is greater than  $0.5 \mu\text{m}$ , brought or joined together mechanically. For thermal contact resistance, readers are referred to a recent comprehensive review by Yovanovich [75]. Originally, TBR refers to the resistance at the interface between two solids or between a liquid and a dielectric at low temperatures. Even when the materials are in perfect contact with each other, reflections occur when phonons travel toward the boundary, because of the difference in acoustic properties of adjacent materials. In practice, the interface can be atomically smooth, or with a roughness ranging from several tenths of a nanometer to several nanometers. The thermal resistance between a solid material and liquid helium is called the Kapitza resistance, first observed by the Russian physicist and 1978 Nobel Laureate Pyotr Kapitza, in the 1940s. The existence of a thermal resistance gives rise to a temperature discontinuity at the boundary and has been modeled, based on the *acoustic mismatch model* (AMM). TBR exists between two dielectrics as well as between a metal and a dielectric. In a thin-film structure, an interface is often accompanied by the formation of an intermediate layer of mixed atoms. An extensive review of earlier studies can be found in the work of Swartz and Pohl [59]. Stoner and Maris [76] used a picosecond thermoreflectance technique to measure the TBR for several metal-dielectric interfaces from 50 to 300 K and observed anomalously large conductance that can be understood as due to the anharmonicity of the metal, resulting in an inelastic channel that facilitated the thermal transport. Phelan and coworkers [77–79] performed extensive research and provided literature survey of TBR of high-temperature superconductors in both the normal and superconducting states, for applications in superconducting electronics and radiation detectors.

Little [60] showed that the heat flux across the boundary of a perfectly joined interface between two solids is proportional to the difference in the fourth power of temperature on each side of the interface. This can be understood based on previous discussions of phonon radiative transfer and blackbody radiation. Consider longitudinal

**Fig. 7.8** Schematic of phonon transport across an interface between two semi-infinite media, each at a thermal equilibrium. Note that arrows at the end denote incidence from the left side, while arrows in the middle denote incidence from the right side



phonon modes that follow the linear dispersion in a Debye crystal, and assume that the interface is perfectly smooth. At any given frequency, the transmission coefficients can be written as follows [60, 77]:

$$\tau_{12} = \tau_{21} = \frac{4\rho_1\rho_2v_{l1}v_{l2}\cos\theta_1\cos\theta_2}{(\rho_1v_{l1}\cos\theta_2 + \rho_2v_{l2}\cos\theta_1)^2} \tag{7.73}$$

where subscripts 1 and 2 denote the media 1 and 2, respectively,  $\rho$  is the density,  $v_l$  is the propagation speed of longitudinal phonons, and  $\theta$  is the polar angle, as illustrated in Fig. 7.8. The scattering is assumed to be purely elastic since the phonon frequency is conserved. An analog of Snell’s law can be written as follows:

$$\frac{1}{v_{l1}}\sin\theta_1 = \frac{1}{v_{l2}}\sin\theta_2 \tag{7.74}$$

Assume  $v_{l1} > v_{l2}$ , for incidence from medium 2 to 1, there exists a critical angle  $\theta_c = \sin^{-1}(v_{l2}/v_{l1})$ , beyond which all phonons will be reflected. Due to the boundary resistance, there will be a temperature difference across the interface. By assuming that the phonons are at equilibrium on either side, the heat flux from medium 1 to 2 can be expressed as follows:

$$q''_{1\rightarrow 2} = \frac{1}{4\pi} \int_0^{\omega_m} \int_0^{2\pi} \int_0^{\pi/2} \hbar\omega v_{l1} f_1(\omega, T_1) \tau_{12} D(\omega) \cos\theta_1 \sin\theta_1 d\theta_1 d\phi_1 d\omega \tag{7.75}$$

If the distribution function is isotropic over the hemisphere, we have

$$q''_{1\rightarrow 2} = \frac{1}{4} \frac{\Gamma_{12}}{v_{l1}^2} \int_0^{\omega_m} \hbar\omega v_{l1}^3 f_1(\omega, T_1) D(\omega) d\omega \tag{7.76}$$

where  $\Gamma_{12}$  can be viewed as the hemispherical transmissivity that is expressed as

$$\Gamma_{12} = \frac{1}{\pi} \int_0^{2\pi} \int_0^{\pi/2} \tau_{12} \cos \theta_1 \sin \theta_1 d\theta_1 d\phi = 2 \int_0^{\pi/2} \tau_{12} \cos \theta_1 \sin \theta_1 d\theta_1 \quad (7.77)$$

It should be noted that

$$\Gamma_{21} = 2 \int_0^{\theta_c} \tau_{21} \cos \theta_2 \sin \theta_2 d\theta_2 = \frac{v_{12}^2}{v_{11}^2} \Gamma_{12} \quad (7.78)$$

One can prove Eq. (7.78) by noting that  $\tau_{21} = \tau_{12}$  and using Eq. (7.74) and its derivative, i.e.,  $v_{11}^{-1} \cos \theta_1 d\theta_1 = v_{12}^{-1} \cos \theta_2 d\theta_2$ . The difference between  $\Gamma_{21}$  and  $\Gamma_{12}$  can be explained as due to total internal reflection since for incidence from medium 2 to 1, portion of the photons will be totally reflected if the incidence angle exceeds the critical angle. For the Debye density of states, we have

$$\frac{1}{4\pi} v_l \hbar \omega f(\omega, T) D(\omega) d\omega = \frac{\hbar \omega^3}{8\pi^3 v_l^2 (e^{\hbar\omega/k_B T} - 1)} \quad (7.79)$$

Therefore, the net heat flux across the interface becomes

$$q_x'' = q_{1 \rightarrow 2}'' - q_{2 \rightarrow 1}'' = \frac{1}{4} \frac{\Gamma_{12}}{v_{11}^2} \int_0^{\omega_m} \hbar \omega [v_{11}^3 f_1(\omega, T_1) - v_{12}^3 f_2(\omega, T_1)] D(\omega) d\omega \quad (7.80a)$$

or

$$q_x'' = \frac{\Gamma_{12}}{v_{11}^2} \frac{k_B^4}{8\pi^2 \hbar^3} \left( T_1^4 \int_0^{x_{m,1}} \frac{x^3 dx}{e^x - 1} - T_2^4 \int_0^{x_{m,2}} \frac{x^3 dx}{e^x - 1} \right) \quad (7.80b)$$

In the low-temperature limit, we obtain

$$q_x'' = \frac{\Gamma_{12}}{v_{11}^2} \frac{\pi^2 k_B^4}{120 \hbar^3} (T_1^4 - T_2^4) \quad (7.81)$$

After replacing  $v_{11}^{-2}$  with  $\sum_j v_{j1}^{-2} = v_{11}^{-2} + 2v_{t1}^{-2}$ , i.e., one longitudinal and two transverse phonon modes, we obtain

$$q_x'' = \frac{\pi^2 k_B^4}{120 \hbar^3} (T_1^4 - T_2^4) \Gamma_{12} \sum_j v_{j1}^{-2} \quad (7.82)$$

The TBR can now be obtained as  $R_b'' = (T_1 - T_2)/q_x''$ . Furthermore, by assuming that the temperature difference is small, we can approximate  $R_b''$  by

$$R_b'' = \frac{30\hbar^3 T^{-3}}{\pi^2 k_B^4 \Gamma_{12} \sum_j v_{j1}^{-2}} \quad (7.83)$$

which is inversely proportional to  $T^3$ . Equations (7.82) and (7.83) are the results of the AMM.

The characteristic wavelength is the most probable wavelength in the phonon distribution function. It can be approximated by

$$\lambda_{\text{mp}} \approx a \frac{\Theta_D}{T} \quad (7.84)$$

where  $a$  is the lattice constant, on the order of 0.3–0.6 nm [77]. Only when  $\lambda_{\text{mp}} \gg \sigma_{\text{rms}}$ , we can assume that the scattering is completely specular. Even for atomically smooth interfaces, the characteristic wavelength for phonons will be on the same order of magnitude as the rms surface roughness, when the temperature approaches the Debye temperature. The specularity parameter was introduced in Chap. 5, Eq. (5.143) and repeated here for normal incidence:

$$p = \exp\left(-\frac{16\pi^2 \sigma_{\text{rms}}^2}{\lambda^2}\right) \quad (7.85)$$

This equation has been wrongly expressed in some literature with  $\pi^2$  being mistaken as  $\pi^3$  due to a typo in an earlier work. In the high-temperature limit, TBR is expected to be small, especially when compared with conduction in the solids. Other considerations are (a) the interface may not be perfectly smooth, (b) there exists an upper limit of the frequency or a lower limit of wavelength, and (c) phonons on either side of the boundary may not be in a local-equilibrium state. These difficulties post some real challenges in modeling TBR. Nevertheless, we shall present the *diffuse mismatch model* (DMM) that was introduced by Swartz and Pohl [59]. In the DMM, it is assumed that phonons will be scattered according to a probability, determined by the properties of the two media but independent of where the phonons originate from. For phonons coming from medium 1, the transmission and reflection probabilities are related by  $\Gamma_{12} + R_{12} = 1$ . For phonons originating from medium 2, on the other hand,  $\Gamma_{21} = R_{12}$  and  $R_{21} = \Gamma_{12}$ . Hence, the reciprocity requires that

$$\Gamma_{12} + \Gamma_{21} = 1 \quad (7.86)$$

We can rewrite Eq. (7.78), considering all three polarizations, as follows:

$$\Gamma_{12} \sum_j v_{j1}^{-2} = \Gamma_{21} \sum_j v_{j2}^{-2} \quad (7.87)$$

The combination of Eqs. (7.86) and (7.87) gives

$$\Gamma_{12} = \frac{\sum_j v_{j2}^{-2}}{\sum_j v_{j1}^{-2} + \sum_j v_{j2}^{-2}} \quad (7.88)$$

This is the DMM prediction of the “hemispherical” transmission coefficient. The heat flux can be calculated according to

$$q_x'' = \frac{k_B^4}{8\pi^2 \hbar^3} \left( T_1^4 \int_0^{x_{m,1}} \frac{x^3 dx}{e^x - 1} - T_2^4 \int_0^{x_{m,2}} \frac{x^3 dx}{e^x - 1} \right) \Gamma_{12} \sum_j v_{j1}^{-2} \quad (7.89)$$

Equations (7.88) and (7.89) are the only equations needed to calculate TBR in the DMM. In addition to the Debye temperatures and the speeds of longitudinal and transverse waves, one would need to determine the upper limits of the integrals in Eq. (7.89). Alternatively, Eq. (7.89) can be recast using the volumetric heat capacity and the group velocity to obtain

$$q_x'' = \frac{1}{4} (C_{v1} v_{g1} T_1 - C_{v1} v_{g1} T_2) \Gamma_{12} \quad (7.90)$$

One must be careful in applying the heat capacity in Eq. (7.80) since the heat capacity in the expression of thermal conductivity is different from  $\rho c_p$ , unless at very low temperatures. Both AMM and DMM assume that phonons on each side of the interface are individually at equilibrium, and do not take into account the nonequilibrium distribution of phonons near the interface. In multilayer thin films, especially in quantum wells and superlattices, when the film thickness is comparable with or smaller than the phonon mean free path, thermal transport inside the film cannot be modeled as pure diffusion anymore. A detailed treatment of temperature-jump conditions and boundary resistance in superlattices can be found from Refs. [61–65]. Majumdar [80] proposed a modified AMM, by modeling interface roughness, using a fractal structure and assuming that the reflection can be approximated by geometric optics which is applicable when the phonon wavelength is smaller than the autocorrelation length of the rough surface. TBR between highly dissimilar materials, metal–metal interface, and metal–dielectric interface has also been extensively studied [47, 48, 81, 82].

### 7.2.4 Atomistic Green’s Function (AGF)

As mentioned previously, the Monte Carlo method has been used extensively for solving the phonon transport equations [57, 58, 83–85]. The lattice Boltzmann method has also been employed in a number of publications [22, 67, 86]. Equilibrium and nonequilibrium molecular dynamics approaches have also been extensively

employed to study thermal transport in nanostructures and TBR [82]. The basics of molecular dynamics simulation of solids have been discussed in Chap. 6 and can be found from the literature [87–95]. Another method called the nonequilibrium Green’s function (NEGF) method has been extensively used to model the electron transport in semiconductor nanodevices [96] and has been introduced to study phonon transport across various interfaces, which is called the atomistic Green’s function (AGF) method [97–99]. The AGF method is briefly discussed in the following.

The NEGF is an atomic-level quantum mechanical model based on the density matrix that can be obtained from the Hamiltonian matrix. As discussed in Sect. 5.6, the electrical current can be expressed in terms of Landauer’s formalism, where the transmission probability can be obtained from the Green’s function formulation [96]. Ozpineci and Ciraci [100] developed the Green’s function method for thermal conductance in a phononic system that consists of chain of atoms between two reservoirs. Mingo and Yang [97] further developed the AGF approach and used it to study phonon transmission through coated nanowires by neglecting inelastic scattering. This method is further extended to study Si/Ge interfaces using an empirical interatomic potential that includes the strain effect [98]. A plane-wave formulation based on the wavevector space is developed to evaluate the harmonic matrix for a unit cell in the  $x$ - $y$  plane and multilayers in the  $z$ -direction across the interface (from left to the right). Green’s function is used to represent the response of the dynamic system to an infinitesimal perturbation and can be used to obtain the transmission coefficient, which is a function of the frequency and parallel wavevector.

$$\Xi(\omega, \mathbf{k}_{\parallel}) = \text{Trace}[\Gamma_L \mathbf{G} \Gamma_R \mathbf{G}^{\dagger}] \quad (7.91)$$

Here,  $\mathbf{k}_{\parallel}$  is the wavevector parallel to the interface, the matrices  $\Gamma_L$  and  $\Gamma_R$  represent the phonon escape rate at the left and right contacts,  $\mathbf{G}$  is a suitable Green’s function matrix, and superscript “ $\dagger$ ” denotes conjugate transpose. The symbol  $\Xi$  is the transmission coefficients for all phonon modes or polarizations. The determination of these matrices requires knowledge of the harmonic matrix and interatomic potentials, and is rather complicated [98, 99]. The heat flux can be obtained based on Landauer’s formalism by integration over the frequency and wavevector space, which can be performed through numerical discretization [98]. The thermal conductance can be obtained as the ratio of the heat flux to the temperature difference. Some studies have separately obtained the polarization-dependent transmission coefficients [101, 102].

While lattice dynamics has been applied to calculate the phonon transport across interfaces [103, 104], it is difficult to implement for various geometric and boundary conditions. Both the lattice dynamics and AGF methods treat phonons as waves and study the coherent propagation, reflection, and transmission of lattice waves through thin films, nanostructures, and interfaces. Similar to the lattice dynamics method, the AGF method is based on the harmonic matrix of the system that can be related to the derivatives of the total interatomic potential. In the AGF method, only the equilibrium positions of the atoms and interatomic force constants (IFCs) are needed. As discussed in Sect. 6.6, the IFCs can be obtained from first-principles

calculations. Most AGF simulations have only dealt with harmonic vibrations, and thus are applicable at temperatures much lower than the Debye temperatures of the materials involved. Molecular dynamic simulations are inherently time domain. The wave-packet method can be applied to molecular dynamics simulations to extract the lattice vibration parameters, such as the mode-specific transmissivity. Due to the fact that molecular dynamics can inherently include anharmonic scattering, it is mostly suitable at high temperatures. On the other hand, standard molecular dynamics employs the Boltzmann distribution for phonons and therefore is not valid at temperatures much lower than the Debye temperature. Therefore, the AGF method and the MD method each has its own advantages depending on the temperature range of interest. Recently, Sadasivam et al. [105] modeled thermal transport across metal silicide and silicon interface using first-principles AGF, and included the anharmonic phonon scattering by modifying the conventional recursive Green's function approach. The AGF method has been used to model coherent phonon across Si/Ge superlattices [106] as well as TBR across stacked graphene/hexagonal boron nitride (hBN) heterostructures [107].

### 7.3 Heat Conduction Regimes

There has been a continuous effort to delineate the regimes of microscale heat conduction since 1992 as discussed in the previous chapters. Nonequilibrium phonon transport in dimensions less than 100 nm has become an important issue in silicon-on-insulator transistors. Multiscale and multiphysics simulations have been developed and applied to nanoelectronic devices [48, 66, 67, 82, 95, 108–110]. This section presents a regime map for heat conduction in solids by electrons and phonons, as schematically depicted in Fig. 7.9. Here, the timescale  $\tau_c$  is known as *effective collision interaction time*, since collision does not occur instantaneously but is through intermolecular potential and force interactions. These forces become important only when the particles become very close to each other. Of course, this is the classical picture of atomic or molecular interactions. Electrons and phonons are quantum mechanical particles; thus, the interaction is via the wavefunctions predicted by Schrödinger's equations. For ultrafast pulse heating, the collision time can be the time required for a photon and an electron to interact. Generally speaking, the relaxation time is much shorter than the relaxation time and neglected in the BTE. The characteristic phonon or electron wavelength  $\lambda$  is assumed to be less than the mean free path  $\Lambda$ .

Region 1 is the macroscale regime where Fourier's law and the heat diffusion equation can be applied, when the timescale is greater than  $\tau$  and the length scale is greater than about  $10\Lambda$ . Region 2 is called the mesoscale or quasi-equilibrium regime, which is characterized by the classical size effect. This region is also known as the first microscale. For heat transfer along with a film or a wire, local-equilibrium assumption is appropriate and boundary scattering reduces the effective mean free path and thermal conductivity. For heat transfer across a film or a multilayer, it is possible

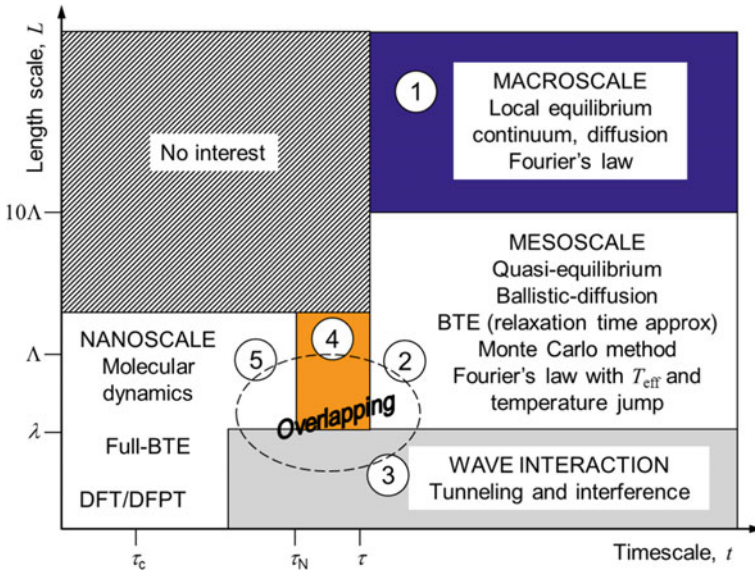


Fig. 7.9 Heat conduction regimes

to use Fourier’s law inside the medium by considering an effective temperature and the temperature-jump boundary condition. It is difficult, if not impossible, to apply Fourier’s law to complex geometries or local heating. The two-temperature model for fast laser heating can be in either region 1 or 2, depending on how the length scale is compared with the mean free path. Most of the research on microscale heat transfer between 1990 and 2005 dealt with the microscale phenomena in region 2.

Region 3 is the regime of wave behavior, which is described by Schrödinger’s wave equations and where quantum tunneling can occur. Quantum size effect becomes significant on thermal conductivity and specific heat. Quantum conductance is a special case of quantum tunneling, for which the ballistic processes are confined in one dimension through a channel. For very thin layers, wave interference and coherent phonon effects may become important. However, due to the interface roughness, the coherence may be destroyed so that the energy ray method or the particle approach can still be applied at very small length scales. We will give a comprehensive treatment of electromagnetic wave interference and scattering phenomena in subsequent chapters. The region on the upper left is said to be of no interest at short timescales because a thermal disturbance cannot travel that far and affect the temperature field.

Region 4 is designed to represent the wavelike behavior, described by the Jeffreys-type equation, Eq. (7.17). When we say Jeffreys-type equation, we mean that both  $\kappa_0$  and  $\kappa_1$  in Eq. (7.16a) are positive. As discussed earlier,  $\tau_N$  is the second relaxation time for phonon scattering that does not transfer or dissipate thermal energy, as in the  $N$  processes. In this regime, the BTE based on the two-relaxation-time

approximation may be applied [31, 32]. This regime includes the heat pulse propagation and the second sound in dielectric crystals, at low temperatures. It suffices to say that this region, while of great academic interest, has very limited applications. The pure hyperbolic heat equation, however, predicts a nonphysical wavefront and cannot be applied without the additional diffusion term. Nevertheless, theoretical studies of the hyperbolic heat equation have helped in better understanding heat transfer behavior on short timescales and, subsequently, facilitated the development of more realistic models. While the lagging heat equation can mathematically describe both wavelike behavior and parallel heat conduction, it does not provide much new physics. On the other hand, the memory concept may be related to the anharmonic and nonlinear effects that are inherent to the solid and crystal structures. Study of the thermomechanical and thermoelastic effects, and thermal transport in polymers and inhomogeneous materials, such as biological materials, may require empirical and semiempirical models. The lagging heat equation or similar differential equations may be quite helpful in these applications.

Region 5 belongs to the nanoscale regime, where it is necessary to employ quantum or sometimes classical molecular dynamics to study the underlying phenomena. At the very fundamental level, DFT and DFPT are needed that can be coupled with molecular dynamics or the first-principles-based BTE as discussed in the previous chapter. The dashed ellipse indicates the overlapping between different regions, where molecular dynamics simulation may provide rich information as well as a bridge between different timescales and length scales.

## 7.4 Thermal Metrology

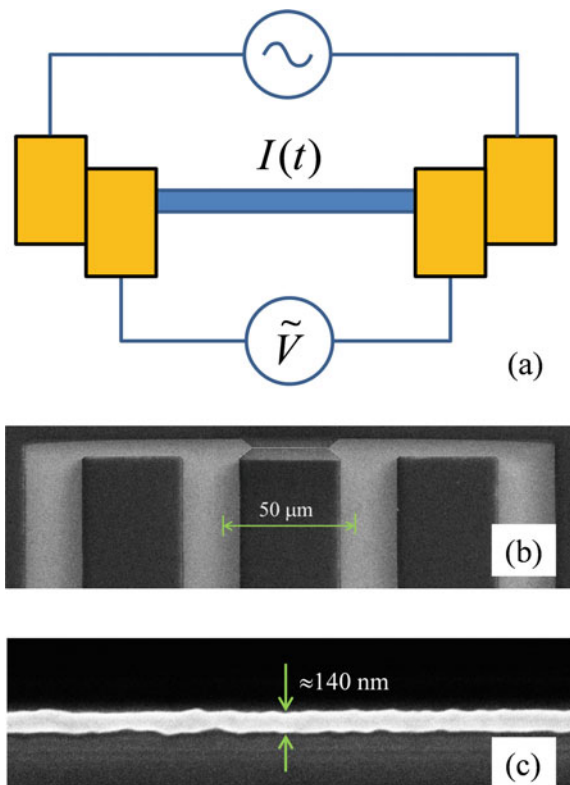
Thermal metrology plays an important role not only in determining the unique properties but also in testing the theoretical predictions and helping to understand the fundamental mechanisms. Thermal metrology includes measurements of temperature (thermometry), specific heat (calorimetry), and heat flux. Thermophysical properties, such as thermal conductivity, thermal diffusivity, and specific heat, can be measured with steady-state, periodically modulated, pulsed, and combined techniques [111–115]. MEMS and NEMS have enabled the fabrication of miniaturized heaters and sensors. Furthermore, optical techniques such as thermoreflectance, Raman spectroscopy, photothermal radiometry, fluorescence, and laser flash techniques have been widely used in the measurement of temperature [116] and thermal properties of nano/microstructured materials [117]. Scanning thermal microscopy and near-field optical microscopy have further improved the spatial resolution [47, 118]. A large number of publications can be found from the bibliography of the previous and present chapters and references therein. A brief overview of selected measurement techniques is given in the following.

### 7.4.1 Microbridge and Suspended Microdevices

The four-point probing microbridge shown in Fig. 7.10 is commonly used for measuring thermal properties. The metal bridge can serve as either a heater or thermometer or both. Platinum (Pt) is mostly used due to its relatively high resistivity, large temperature coefficient of resistance (TCR), and chemical stability. Either steady-state, transient, or periodic-heating methods can be used in the measurements; in some cases, a combined heating method can be used alternatively or simultaneously. The microbridge can be fabricated on a dielectric substrate, a thin insulating film on a substrate, or a suspended membrane, allowing both in-plane and cross-plane thermal transport properties to be measured. The thickness of the metal film is typically several tens of nanometers and the width of the bridge can vary from tens of nanometers to several micrometers. Depending on the applications, the bridge length can vary from tens of micrometers to several millimeters. Extensive discussions on the use of electrothermal techniques for measuring the thermal conductivity and thermal diffusivity can be found from Refs. [47, 112, 119].

As an example, Fig. 7.10b and c display the SEM images of a microfabricated bridge used as a thermometer [120]. The Pt film with a thickness of 35 nm was etched

**Fig. 7.10** A patterned heater/thermometer microbridge in a four-terminal sensing scheme. **a** Schematic of the microbridge circuit; **b** a Pt microbridge with a length of 29  $\mu\text{m}$  connected to four electrodes and **c** portion of the microbridge whose width is approximately 140 nm [120]



using focused ion beam (FIB) to a width of 140 nm over 29  $\mu\text{m}$  length. The bridge was fabricated over a  $\text{SiO}_2$  film on Si substrate for characterizing the heating effect from an AFM cantilever as it approaches and scans the surface. The TCR was calibrated to be near 20% that of bulk Pt, which is approximately  $0.0039 \text{ K}^{-1}$ . The resistivity was about five times that of pure Pt, suggesting grain boundary and geometric boundary scattering effects may play a role in the deposited Pt film and etched microbridge [120]. It is necessary to calibrate the microfabricated thermometers and to determine the TCR curve before performing actual measurements.

Since it often takes a long time to achieve steady states, traditionally, the hot wire and hot strip methods have been developed to measure thermal properties using a step function or a short impulse of electrical power. In the late 1980s, Cahill et al. [121–123] developed the 3- $\omega$  or 3- $\omega$  method for measuring thermal conductivity of amorphous solids and thin films using a lock-in amplifier to generate a harmonic oscillating current signal  $I \sim \cos(\omega t) = \cos(2\pi f t)$  and measure the voltage signal oscillating at a frequency of  $3\omega$ . This method greatly reduces the effect of background effects such as thermal radiation and can be used for both cross-plane and in-plane thermal conductivity. The basic principle is that when an alternating current passes through the bridge as illustrated in Fig. 7.10a at a frequency  $\omega$ , the voltage  $\tilde{V}_\omega = \tilde{I}_\omega R$  also oscillates at a frequency of  $\omega$ . Consequently, the electrical power  $\tilde{P}_{2\omega} = \tilde{I}_\omega \tilde{V}_\omega$  is modulated at  $2\omega$ , which is dissipated as Joule heating to the bridge. The resulting temperature oscillates around the mean temperature at a frequency of  $2\omega$  with a phase delay  $\phi$  that depends on the properties and geometry of the system. The mean temperature (operating temperature) of the bridge depends on the average heating power. The resistance of the bridge is therefore modulated about its operating point at a frequency of  $2\omega$ . The lock-in amplifier collects the voltage signal and performs a frequency analysis to extract the  $3\omega$  voltage signal  $\tilde{V}_{3\omega} = \tilde{I}_\omega \tilde{R}_{2\omega}$ . Through careful models of the heat transfer processes and known parameters such as the film thickness and specific heat capacity, the 3- $\omega$  method has become a powerful technique in measuring thermal conductivity, especially for semiconductors and insulators [47]. Dames [124] gave an extensive review with background information of the 3- $\omega$  methods and its variations. Kommandur and Yee [125] fabricated a microbridge on a suspended semiconducting polymer film and used the 3- $\omega$  method to measure the in-plane thermal conductivity and to characterize the anisotropy in thermal transport properties.

Shi et al. [126] microfabricated suspended devices for measuring thermal and electrical properties of nanostructures. Kim et al. [127] reported the first thermal conductivity measurements of individual carbon nanotubes (CNTs) using a suspended microdevice. Yu et al. [128] measured the thermal conductance and the Seebeck coefficient of an individual single-wall CNT. The device includes two suspended islands made of silicon nitride ( $\text{SiN}_x$ ) membrane and each island is supported by five  $\text{SiN}_x$  beams as shown in Fig. 7.11. A Pt thin film is coated on the membrane and patterned in serpentine winding on each island. The four beams or leads form four contact points that provide heating power and measure the temperature of the island simultaneously. One of the islands is used as the heater (with its own thermometer) and the other island serves as the heat sink. Nanotubes or nanowires with a length of

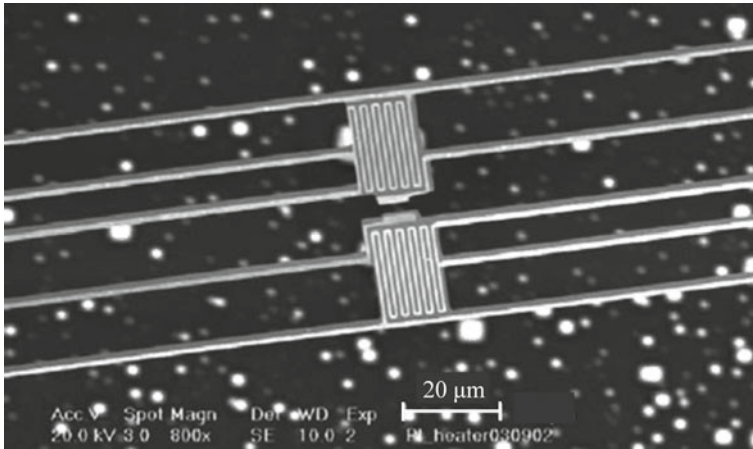


**Fig. 7.11** Schematic of the microfabricated suspended device that has two isolated membranes with patterned Pt resistors supported by silicon nitride beams. *Reprinted with permission from Yu et al. [128]; copyright (2005) American Chemical Society*

about 5–20  $\mu\text{m}$  can be laid between the islands. Additional beams may be used to measure the resistance of the suspended nanotubes, nanowires, and nanofilms [126–130]. Both steady-state and transient measurements have been performed. Detailed analysis of the thermal resistance and the effect of contact resistance need to be taken into consideration; see a recent review by Weathers and Shi [130].

Fujii et al. [131] fabricated a suspended T-shape nanosensor to measure the thermal conductivity of individual CNTs of a few micrometers in length. The Pt strip of a length of 5–6  $\mu\text{m}$ , width on the order of 0.5  $\mu\text{m}$ , and thickness a few tens of nanometers, is suspended. The CNT is suspended from the middle of the Pt strip to a heat sink. Under steady-state operation with DC current, the temperature difference between the ends of the CNT and heat flow rate through the CNT can be determined by analyzing the measurement results to determine its thermal conductivity.

Recently, Kim et al. [132] proposed to use four suspended parallel bridges made of Pt strip on  $\text{SiN}_x$  beams to measure the thermal and thermoelectric properties of nanostructures. Though the analysis involves detailed heat transfer and thermal resistances through the beams, the fabrication is much easier than the suspended islands structures. Furthermore, individual beams can serve as a four-point probe and heater. Contact resistance can also be compensated for through a careful analysis of the thermal resistance network. The setup has been used to measure Si nanowires from 100 to 500 K and BAs microrods from 250 to 350 K [132, 133]. Transient and  $3\omega$  sensing schemes may also be employed to measure the thermal and thermoelectric properties of nanowire structures.

### 7.4.2 Scanning Probe Microscopic Techniques

As mentioned in Chap. 1, the family of scanning probe microscopy (SPM) has been established as a powerful toolbox in nanotechnology from manipulating and imaging single atoms to probing the topological, chemical, and thermal profiles near the interfaces. Majumdar [134] reviewed the development and applications of scanning thermal microscopy (SThM) for local temperature mapping with a few tens of nanometer resolution by fabricating a thermocouple or resistance thermometer. The method was developed by Majumdar et al. [135, 136] in the early 1990s to allow surface temperature measurements based on the previous work at IBM [137]. Another method, also pioneered by Majumdar [138] used the thermal expansion principle called the scanning Joule expansion microscopy, which has been further developed to measure the temperature profile with 10 nm resolution for studying the size effect of thermal conductivity [139] as well as imaging the thermal and thermoelectric characteristics at graphene-metal contact [140]. The most frequently used SThM is based on fabricating a thermocouple at the tip. The method has been further developed through the years not only for local temperature measurements but also for thermal conductivity measurement and thermoelectric property characterization as reviewed in Refs. [141, 142].

A representative high-quality SThM with a thermocouple at the tip is shown in Fig. 7.12, which can be used in air [143]. The probe was made of silica with a very low thermal conductivity, and the tip was made to be 12  $\mu\text{m}$  long to minimize the air gap effect. In addition to measuring the thermal profile for a heated sample, the thermal conductivity profile can be obtained by heating the tip with a high-frequency ( $>100$  kHz) AC current such that a steady-state temperature is sensed by the thermocouple whose time constant is greater than 1 ms [143].

The cantilever tip or cantilever can be optically or electrically heated with controllable temperature for thermal processing, nanofabrication, data writing and reading, and for the study of thermal transport at nanoscales [144, 145]. Lee et al. [146, 147] performed a steady-state and frequency-dependent characterization of heated AFM cantilevers over a range of pressures for thermal metrology applications. The temperature distribution in heated Si cantilevers was obtained with micro-Raman spectroscopy with a spatial resolution of 1  $\mu\text{m}$ . Park et al. [148] analyzed the frequency response of heated AFM cantilevers in the frequency range from 10 Hz to 1 MHz, and observed high-order harmonic responses, such as  $3\omega$ ,  $5\omega$ , and  $7\omega$ , at frequencies below 100 kHz and impedance effects at higher frequencies. Park et al. [149] also investigated thermal behavior of heated cantilevers at cryogenic temperatures, down to 78 K. By measuring the thermal response at various frequencies, this study extracted the specific heat near the cantilever tip and the thermal conductivity along the heavily doped silicon legs, at temperatures ranging from 80 to 200 K. There appears to be a significant reduction in the thermal conductivity for the free-standing silicon cantilever, with a thickness of 0.59  $\mu\text{m}$ , at low temperatures. The heat transfer between heated AFM microcantilever and substrate has also been investigated [120]. As reviewed by King et al. [150], heated AFM cantilevers have become a useful thermal analysis tool at the micro- and nanoscales.

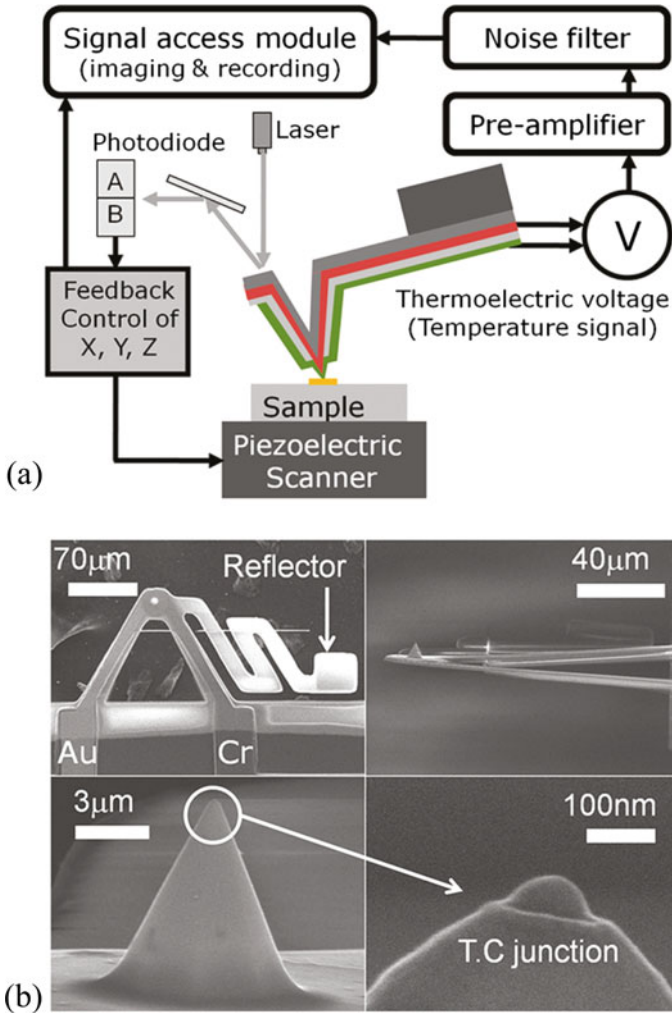


**Fig. 7.12** Scanning thermal microscopy with a special resolution of about 50 nm for temperature and thermal conductivity characteristics.: **a** Schematic of the experimental and the tip layout; **b** SEM images of the probe tip and cantilever. Reprinted with permission from Kim et al. [143]; copyright (2011) American Chemical Society

### 7.4.3 Noncontact Optical Techniques

Optical methods are noncontact and can have a large range of temporal resolutions for measuring temperature and thermal properties such as thermal conductivity, diffusivity, specific heat, thermal boundary resistance, and the electron–phonon coupling constant [116, 117]. Femtosecond lasers have become much more affordable and

accessible in recent years [49, 151–155]. For measurement of bulk and film properties, a temporal resolution of 10 ns–10 ms is usually sufficient. In order to probe thermal boundary resistance between films or thermal properties of very thin films, a resolution of 100 ps–10 ns is frequently used [156–158]. To measure the electron–phonon coupling, ultrafast lasers are needed since picosecond resolution is required [38–46, 159]. Another advantage of optical methods is that the beam spot size can be made relatively small, down to a few micrometers using an objective lens. Sub-micron resolution can be achieved with micro-Raman thermometry. Measurements with 50–500 nm spatial resolution can be made possible using near-field optics or fabricated nanostructures [118, 160–162].

Pump-and-probe methods are often employed in which the sample surface is heated by a laser beam (or another optical source) and the thermal responses are measured using one of the variety of probing techniques. Examples are the thermoreflectance method based on the temperature dependence of the reflectance of the surface or film, micro-Raman thermometry based on the Raman shift due to phonon scattering being temperature dependent, the radiometric method based on the thermal emission signal according to the theory of blackbody radiation, and photoacoustic and photodeflection techniques [112, 113, 117]. Measurements are often accomplished either in the time domain, when the transient thermal response after pulsed or step heating is observed, or in the frequency domain, when periodic heating is used and the periodic response with a time delay is measured [47, 112, 117]. The latter is also called the thermal wave method [11, 12].

Figure 7.13 illustrates a time-domain thermoreflectance (TDTR) setup [154] for measuring the thermal conductivity of film or bulk materials as well as TBR. The pump-probe scheme is shown in Fig. 7.13a. The transducer is usually a metal film. The thermoreflectance coefficient is defined as follows

$$C_{\text{TR}} = \frac{1}{R} \frac{\partial R}{\partial T} \quad \text{or} \quad \frac{\Delta R}{R} = C_{\text{TR}} \Delta T \quad (7.92)$$

The temperature and wavelength dependence of  $C_{\text{TR}}$  of metal films have been extensively characterized [163]. For Au, due to the interband transition near the wavelength of  $\lambda = 500$  nm, the absorbance and thermoreflectance coefficient is relatively large. For Al, the absorbance is high near  $\lambda = 800$  nm. The wavelength of pulsed Ti-sapphire lasers ranges from 720 to 880 nm; thus, Al coating is typically used [49, 159]. The pulse duration is typically 90–150 fs, though shorter pulses can also be generated using a mode-locking technique. As shown in Fig. 7.13b, the laser beam after the optical isolator is split into a pump beam (high power) and a probe beam (low power) using a polarizing beamsplitter (PBS). The output of the laser is a pulse train at a typical frequency of 80 MHz. An electro-optic modulator (EOM) is used to reduce the modulation frequency to 1–10 MHz range for measuring thermal properties or TBR. The probe beam goes through a delay stage in order to probe the sample temperature after the pump pulse heating. Both beams are sent to the sample through the objective lens. After averaging over many pulses, the delay stage is moved to vary the delay time. It should be noted this method is different from the traditional

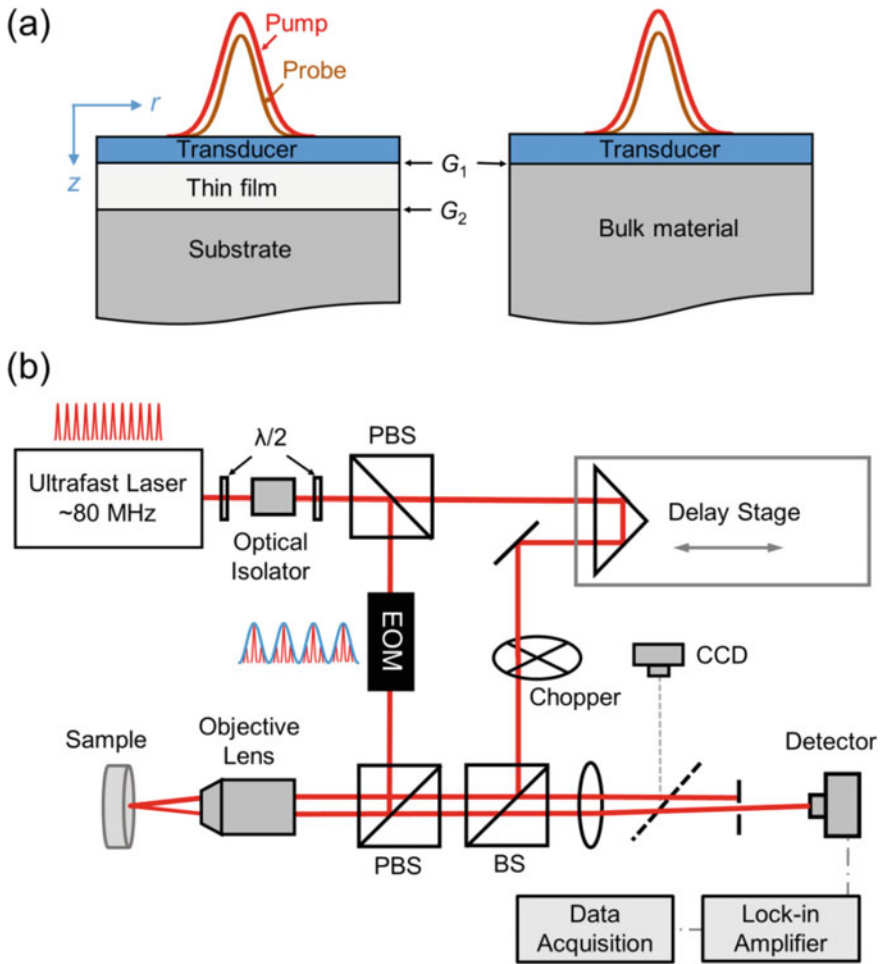


**Fig. 7.13** Schematic of a TDTR: **a** Illustration of the pump and probe beams on a sample; **b** the optical layout. Reprinted with permission from Jiang et al. [154]; copyright (2018) AIP Publishing

transient response method. For example, in the conventional transient laser heating and relaxation method, the temperature rise and fall after the laser pulse is monitored continuously with a temporal resolution typically from 1  $\mu\text{m}$  to 1 ms [112]. In a TDTR measurement, the response at each delay step is recorded and then plotted as a function of time. The delay step determines the temporal resolution which can be varied from tens of femtoseconds to tens of picoseconds. Since the movement of the delay stage can be precisely controlled with a micrometer resolution, the smallest time delay that can be achieved is less than 10 fs. For example, if the total travel length of the delay stage is 30 cm, the maximum delay time is 2 ns. In some experimental setups, a forward advance is used for the pump beam rather than

delaying the probe beam. The chopper may be used to vary the frequency of the probe beam independently for dual-frequency measurement [154, 164]. A second harmonic generator can be used to double the frequency of either the pump beam or probe beam so that its wavelength is changed to the visible range [49]. TDTR methods have been used to measure the thermal conductivity accumulation function in terms of the mean free path [151, 152] as well as the thermal conductivity of perforated membranes [165, 166]. Wagner et al. [166] also used a two-laser setup with a micro-Raman thermometer at submicron resolution to obtain the steady-state temperature profile during continuous laser heating.

By changing the beam size and modulation frequency, it is possible to determine both in-plane and cross-plane thermal conductivity by fitting the model prediction to the experimental data using the least-squares method. Another way to probe the in-plane thermal transport is to use a lateral offset between the pump beam and the probe beam. Wang et al. [167] used both methods to study the thermal conductivity of layered borides. To measure the properties of 2D materials it is critically important to reduce the metal layer thickness. A magneto-optical thin film (on the order of 20 nm) has been used as the transducer. Under a magnetic field due to the Kerr effect, the polarization of the reflected beam is a function of temperature. The method based on time-resolved magneto-optical Kerr effect (TR-MOKE) has been developed and used to measure the anisotropic thermal conductivity of molybdenum disulfide [168] and black phosphorus [153].

The femtosecond laser setup can be used for frequency-domain thermoreflectance (FDTR) with few hardware modifications [169]. The signal reaching the detector, or the reflection of the probing beam, is at the same frequency as the pump beam with a phase delay [151]. The modulation frequency is determined by the EOM and can be varied from 25 kHz to 20 MHz. By fixing the time delay and changing the modulation frequency, one can obtain the frequency response. Theoretical models are necessary to relate the frequency response to the properties being determined [169]. FDTR can also be performed with two continuous-wave lasers [169–171]. Regner et al. [170] developed a two-laser FDTR setup to measure the phonon mean free spectra for crystalline Si, doped Si, amorphous Si, and amorphous SiO<sub>2</sub>.

A modified setup is used to measure anisotropic thermal conductivity of thin films, as shown in Fig. 7.14 [171]. Two continuous-wave green lasers at slightly different wavelengths are used. The wavelengths of 488 nm and 532 nm match well with the peaks of absorption and thermoreflectance coefficients of the gold film (transducer), respectively [163]. An optical isolator (ISO) is used after each laser to prevent the reflected beam from reentering the laser cavity. After a half-wave plate (HWP), the pump beam is modulated by EOM at frequency  $f$ , which can be varied in a large range from about 9 kHz to 200 GHz, though only the middle range is useful for the data analysis and parameter reduction. A piezomotor mirror, which uses a piezoelectric actuator to fine tune the angular rotation, is used to offset the probe beam position. After the beamsplitter (BS), both beams go through the PBS, a quarter-wave plate (QWP), and the objective lens (OBJ) to focus on the sample surface. Only reflected light at the probe beam frequency is allowed to enter the photodetector (PD) thanks to a bandpass filter (BP). The detector receives a signal

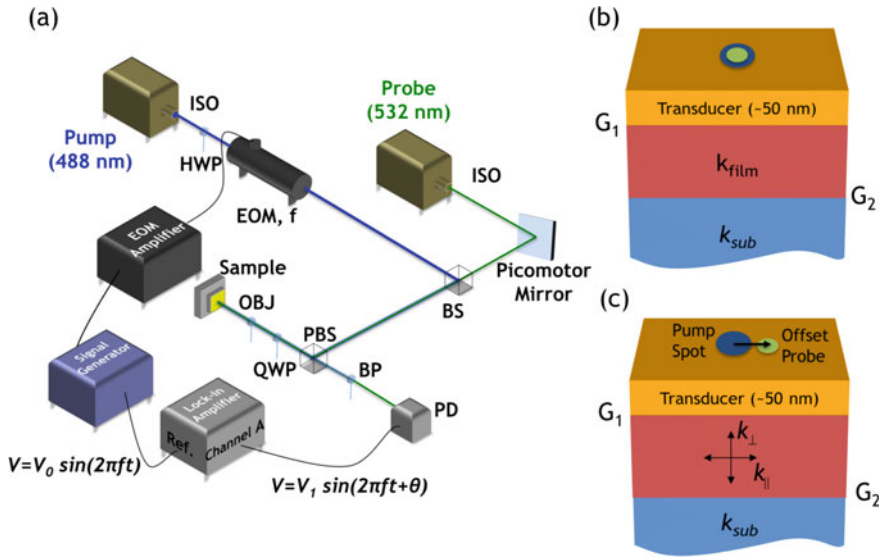


**Fig. 7.14** Illustration of a frequency-domain thermoreflectance measurement system and scenarios. **a** The optical layout of the two-laser FDTR setup; **b** scheme for measuring thermal conductivities of the film, substrate, and TBR,  $G_1$  and  $G_2$ , with concentrated beams; **c** scheme for measuring anisotropic thermal conductivities, both in-plane  $k_{\parallel}$  and cross-plane  $k_{\perp}$ , of the film with an offset beam spot. Reprinted with permission from Rodin and Yee [171]; copyright (2017) AIP Publishing

due to the temperature change of the sample at the same frequency  $f$  but with a phase lag  $\phi$ , which depends on the materials properties, lateral offset, and the modulation frequency  $f$ . The phase lag can be measured with a lock-in amplifier using either a heterodyne modulator [170] or a signal generator [171]. Through careful thermal modeling and a least-squares fitting, the desired properties such as the TBR, in-plane and cross-plane thermal conductivities of the film can be determined. The results for crystalline and amorphous  $\text{Al}_2\text{O}_3$  and  $\text{SiO}_2$ , respectively, along with highly oriented pyrolytic graphite have been reported [171].

The femtosecond transient thermal grating (TTG) method has also been used for measuring the thermal conductivity accumulation functions of thin membranes [172–174]. A pulsed laser (wavelength 515 nm and pulse width 60 ps) is split into beams using diffraction optics and then focused to the sample, causing sinusoidal interference patterns on the sample, which can be a thin film or membrane. A continuous laser is either reflected or transmitted through the sample, producing a diffraction signal whose decay is related to the thermal diffusivity. Silicon membranes of thicknesses from 1500 nm down to 17.5 nm have been measured to demonstrate ballistic thermal transport as well as to study the thermal conductivity accumulation function [172, 173]. Transport along perforated silicon membrane has also been examined [174].

## 7.5 Summary

The present chapter, together with Chaps. 5 and 6, provides a comprehensive treatment of thermal properties of and transport processes in micro/nanostructured solid materials. This chapter focused on the transient and nonequilibrium heat conduction, when the local-equilibrium condition is not satisfied to justify the conventional heat diffusion theory, based on Fourier's law. Several modified phenomenological theories were critically reviewed with an emphasis on their application regimes. The phonon BTE was presented using the EPRT, and the solutions were discussed for the nonequilibrium heat transfer across a thin film or a multilayer structure. The basic models of TBR were outlined. A summary on the advanced atomistic scale modeling is provided focusing on the atomistic Green's function method. A heat transfer regime was developed to assist readers in choosing an appropriate methodology for a given situation. Finally, some important thermal measurement techniques are discussed with extensive references.

## Problems

- 7.1. What are the characteristic lengths for heat conduction along a thin film? Why is local equilibrium a good assumption in this case, even though the film thickness is less than the mean free path of heat carriers? Why does the thermal conductivity depend on the thickness of the film?
- 7.2. Why do we say that Fourier's law is a fundamental physical law, like Newton's laws in mechanics, but Cattaneo's equation is not? Comment on the paradox of infinite speed of heat diffusion by considering the feasibility of exciting the surface temperature or depositing a heat flux to the surface instantaneously.
- 7.3. Consider a 1D semi-infinite medium, initially at uniform temperature  $T_i$ , where the surface temperature is suddenly changed to a constant temperature,  $T(0, t) = T_s$ . The analytical solution of the heat diffusion equation gives  $\theta(x, t) = \frac{T(x, t) - T_i}{T_s - T_i} = \text{erfc}\left(\frac{x}{2\sqrt{\alpha t}}\right)$ . For silicon at various temperatures, use the properties given in Example 5.6 to estimate how long it will take for a given location to gain a temperature rise that is  $10^{-12}$ , or one part per trillion of the maximum temperature difference. Estimate the average thermal diffusion speed in terms of  $x$  and  $T_i$ . Hint:  $\text{erfc}(5.042) = 1.00 \times 10^{-12}$ .
- 7.4. Repeat Problem 7.3, using copper instead of silicon as the material, based on the properties given in Example 5.5. Discuss why the average thermal diffusion speed is different under different boundary conditions, i.e., constant heat flux and constant temperature. From an engineering point of view, do you think heat diffusion is a fast or slow process? Why?
- 7.5. (a) Derive Eq. (7.4), the hyperbolic heat equation from Cattaneo's equation  
 (b) Derive Eq. (7.14), the lagging heat equation, based on the dual-phase-lag model.

- 7.6. Take GaAs as an example. How would you compare the speed of sound with the average thermal diffusion speed, at different temperatures and length scales? This problem requires some literature search on the properties.
- 7.7. Assume the hyperbolic heat equation would work for transient heat transfer in glass (Pyrex), at room temperature. Given  $\kappa = 1.4 \text{ W/m K}$ ,  $\rho = 2500 \text{ kg/m}^3$ ,  $c_p = 835 \text{ J/kg K}$ , and  $v_a = 5640 \text{ m/s}$ .
- At what speed would the temperature wave propagate?
  - For an excimer laser with a pulse width  $t_p = 10 \text{ ns}$ ,  $0.1 \text{ ns}$  after the pulse starts, could the hyperbolic equation be approximated by the parabolic equation?
  - Suppose we have an instrument available to probe the timescale below  $\tau_q$ , will the hyperbolic heat equation be able to describe the observation?
- 7.8. Derive Eq. (7.13b) from Eq. (7.13a). Discuss the conditions for these equations to be reduced to Fourier's law or Cattaneo's equation.
- 7.9. Show that Eq. (7.17) satisfies Eq. (7.16). Discuss the conditions for Eq. (7.17) to represent Fourier's law or Cattaneo's equation.
- 7.10. Derive Eqs. (7.18a), (7.18b), and (7.18c).
- 7.11. Derive Eqs. (7.27a) and (7.27b). Calculate  $\tau$ ,  $\tau_q$ , and  $\tau_T$  of copper, for  $T_e = 300, 1000, \text{ and } 5000 \text{ K}$ , assuming the lattice temperature  $T_s = 300 \text{ K}$ .
- 7.12. Calculate the electron-phonon coupling constant  $G$  for aluminum, copper, gold, and silver, near room temperature. Discuss the dependence of  $\kappa$  and  $G$  upon the electron and lattice temperatures  $T_e$  and  $T_s$ .
- 7.13. At  $T_e = 1000, 3000, \text{ and } 6000 \text{ K}$ , estimate the energy transfer by thermionic emission from the copper surface, assuming that the electrons obey the equilibrium distribution function at  $T_e$ .
- 7.14. Based on Example 7.3, evaluate the heat flux in a thin silicon film. How thin must it be in order for it to be considered as in the radiative thin limit? Calculate the medium temperature  $T$ . Plot the left-hand side and the right-hand side of Eq. (7.43). Furthermore, assuming Eq. (7.43) to be true for each frequency, find a frequency-dependent temperature  $T(\omega)$  of the medium. At what frequency does  $T(\omega) = T$ ? Is there any physical significance of  $T(\omega)$ ?
- 7.15. Derive Eq. (7.53), using Eqs. (7.38), (7.49a), (7.49b), and (7.50).
- 7.16. In principle, one should be able to study nonequilibrium electrical and thermal conduction in the direction perpendicular to the plane and use the BTE to determine the effective conductivities. This could be a team project, for a few students, to formulate the necessary equations. As an individual assignment, describe how to set up the boundary conditions, as well as the steps you plan to follow, without actually deriving the equations.
- 7.17. For a diamond type IIa film,  $v_l = 17,500 \text{ m/s}$ ,  $v_t = 12,800 \text{ m/s}$ , and  $\kappa = 3,300 \text{ W/m K}$ , near  $300 \text{ K}$ . Assume that the boundaries can be modeled as blackbodies for phonons. For boundary temperatures  $T_1 = 350 \text{ K}$  and  $T_2 = 250 \text{ K}$ , calculate and plot the heat flux  $q_x''$  and the effective thermal conductivity  $\kappa_{\text{eff}}$  across the film of thickness  $L$ , varying from  $0.05$  to  $50 \mu\text{m}$ .

- 7.18. Calculate the TBR between high-temperature superconductor  $\text{YBa}_2\text{Cu}_3\text{O}_{7-\delta}$  and MgO substrate, at an average temperature between 10 and 90 K, using both the AMM and the DMM without considering the electronic effect. The following parameters are given for  $\text{YBa}_2\text{Cu}_3\text{O}_{7-\delta}$ :  $v_l = 4780$  m/s,  $v_t = 3010$  m/s,  $\rho = 6338$  kg/m<sup>-3</sup>, and  $\Theta_D = 450$  K; and for MgO:  $v_l = 9710$  m/s,  $v_t = 6050$  m/s,  $\rho = 3576$  kg/m<sup>-3</sup>, and  $\Theta_D = 950$  K.
- 7.19. Evaluate the effective thermal conductivity near room temperature of a GaAs/AlAs superlattice, with a total thickness of 800 nm, using the DMM to compute the transmission coefficient. Assume the end surfaces are blackbodies to phonons; consider that (a) each layer is 4 nm thick and (b) each layer is 40 nm thick. The following parameters are given, considering phonon dispersion on thermal conductivity, for GaAs:  $C = 880$  kJ/m<sup>3</sup> K,  $v_g = 1024$  m/s, and  $\Lambda = 145$  nm; and for AlAs:  $C = 880$  kJ/m<sup>3</sup> K,  $v_g = 1246$  m/s, and  $\Lambda = 236$  nm. How is the result compared with a single layer of either GaAs or AlAs?
- 7.20. Evaluate the effective thermal conductivity near room temperature of a Si/Ge superlattice, with a total thickness of 1000 nm, using the DMM to compute the transmission coefficient. Assume the end surfaces are blackbodies to phonons; consider that (a) each layer is 5 nm thick and (b) each layer is 50 nm thick. The following parameters are given, considering phonon dispersion on thermal conductivity, for Si:  $C = 930$  kJ/m<sup>3</sup> K,  $v_g = 1804$  m/s, and  $\Lambda = 260$  nm; and for Ge:  $C = 870$  kJ/m<sup>3</sup> K,  $v_g = 1042$  m/s, and  $\Lambda = 199$  nm. How is the result compared with a single layer of either Si or Ge?
- 7.21. Make a comparison of the different methods for measuring the thermal conductivity of a thin film.
- 7.22. Suppose one wishes to measure the thermal conductivity of a graphene sheet of  $10 \mu\text{m} \times 10 \mu\text{m}$ , what method(s) would you recommend?
- 7.23. Suppose one wishes to measure the thermal conductivity of a superlattice Si/Ge nanowire of length  $50 \mu\text{m}$  and diameter 3 nm, what method would you suggest?
- 7.24. What is the mechanism of transient thermal grating? What properties can be measured by the TTG method?

## References

1. H.S. Carslaw, J.C. Jaeger, *Conduction of Heat in Solids*, 2nd edn. (Clarendon Press, Oxford, 1959)
2. M.N. Özışık, *Heat Conduction*, 2nd ed., Wiley, New York, 1993; also D.W. Hahn and M.N. Özışık, *Heat Conduction*, 3rd ed., Wiley, New York, 2012
3. T.J. Bright, Z.M. Zhang, Common misperceptions of the hyperbolic heat equation. *J. Thermophys. Heat Transfer* **23**, 601–607 (2009)
4. D. D. Joseph, L. Preziosi, Heat waves. *Rev. Mod. Phys.*, **61**, 41–73 (1989)
5. D.D. Joseph, L. Preziosi, Addendum to the paper ‘heat waves’. *Rev. Mod. Phys.* **62**, 375–391 (1990)

6. D.Y. Tzou, *Macro- to Microscale Heat Transfer: The Lagging Behavior*, 2nd edn. (Wiley, New York, 2015)
7. M.N. Özışık, D.Y. Tzou, On the wave theory in heat conduction. *J. Heat Transfer* **116**, 526–535 (1994)
8. W.K. Yeung, T.T. Lam, A numerical scheme for non-Fourier heat conduction, Part I: one-dimensional problem formulation and applications. *Numer. Heat Transfer B* **33**, 215–233 (1998)
9. A. Haji-Sheikh, W.J. Minkowycz, E.M. Sparrow, Certain anomalies in the analysis of hyperbolic heat conduction. *J. Heat Transfer* **124**, 307–319 (2002)
10. J. Gembarovic, J. Gembarovic Jr., Non-Fourier heat conduction modeling in a finite medium. *Int. J. Thermophys.* **25**, 1261–1268 (2004)
11. C.A. Bennett, R.R. Patty, Thermal wave interferometry: a potential application of the photoacoustic effect. *Appl. Opt.* **21**, 49–54 (1982)
12. A. Mandelis (ed.), *Photoacoustic and Thermal Wave Phenomena in Semiconductors* (Elsevier, Amsterdam, 1987)
13. M.B. Rubin, Hyperbolic heat conduction and the second law. *Int. J. Eng. Sci.* **30**, 1665–1676 (1992)
14. C. Bai, A.S. Lavine, On hyperbolic heat conduction and the second law of thermodynamics. *J. Heat Transfer* **117**, 256–263 (1995)
15. A. Barletta, E. Zanchini, Hyperbolic heat conduction and local equilibrium: a second law analysis. *Int. J. Heat Mass Transfer* **40**, 1007–1016 (1997)
16. D. Jou, G. Lebon, J. Casas-Vázquez, *Extended Irreversible Thermodynamics*, 4th edn. (Springer, Berlin, 2010)
17. Z.M. Zhang, T.J. Bright, G.P. Peterson, Reexamination of the statistical derivations of Fourier's law and Cattaneo's equation. *Nanoscale Microscale Thermophys. Eng.* **15**, 220–228 (2011)
18. J. Tavernier, Sur l'équation de conduction de la chaleur. *Comptes Rendus Acad. Sci.* **254**, 69–71 (1962)
19. A. Majumdar, Microscale heat conduction in dielectric thin films. *J. Heat Transfer* **115**, 7–16 (1993)
20. A.A. Joshi, A. Majumdar, Transient ballistic and diffusive phonon heat transport in thin films. *J. Appl. Phys.* **74**, 31–39 (1993)
21. S. Volz, J.-B. Saulnier, M. Lallemand, B. Perrin, P. Depondt, M. Mareschal, Transient Fourier-law deviation by molecular dynamics in solid argon. *Phys. Rev. B* **54**, 340–347 (1996)
22. J. Xu, X.W. Wang, Simulation of ballistic and non-Fourier thermal transport in ultra-fast laser heating. *Phys. B* **351**, 213–226 (2004)
23. M. Chester, Second sound in solids. *Phys. Rev.* **131**, 2013–2015 (1963)
24. M.E. Gurtin, A.C. Pipkin, A general theory of heat conduction with finite wave speeds. *Arch. Ration. Mech. Anal.* **31**, 113–126 (1968)
25. P.J. Antaki, Solution for non-Fourier dual phase lag heat conduction in a semi-infinite slab with surface heat flux. *Int. J. Heat Mass Transfer* **41**, 2253–2258 (1998)
26. D.W. Tang, N. Araki, Wavy, wavelike, diffusive thermal responses of finite rigid slabs to high-speed heating of laser-pulses. *Int. J. Heat Mass Transfer* **42**, 855–860 (1999)
27. D.Y. Tzou, K.S. Chiu, Temperature-dependent thermal lagging in ultrafast laser heating. *Int. J. Heat Mass Transfer* **44**, 1725–1734 (2001)
28. L.Q. Wang, X.S. Zhou, X.H. Wei, *Heat Conduction: Mathematical Models and Analytical Solutions* (Springer-Verlag, Berlin, 2008)
29. W.J. Minkowycz, A. Haji-Sheikh, K. Vafai, On departure from local thermal equilibrium in porous media due to a rapid changing heat source: the Sparrow number. *Int. J. Heat Mass Transfer* **42**, 3373–3385 (1999)
30. W. Kaminski, Hyperbolic heat conduction equation for materials with a nonhomogeneous inner structure. *J. Heat Transfer* **112**, 555–560 (1990)
31. J. Callaway, Model for lattice thermal conductivity at low temperatures. *Phys. Rev.* **113**, 1046–1051 (1959)

32. R. A. Guyer, J. A. Krumhansl, Solution of the linearized phonon Boltzmann equation. *Phys. Rev.* **148**, 766–778 (1966); Thermal conductivity, second sound, and phonon hydrodynamic phenomena in nonmetallic crystals. *Phys. Rev.* **148**, 778–788 (1966)
33. J. Shiomi, S. Maruyama, Non-Fourier heat conduction in a single-walled carbon nanotube: Classical molecular dynamics simulations. *Phys. Rev. B* **73**, 205420 (2006)
34. D.H. Tsai, R.A. MacDonald, Molecular-dynamics study of second sound in a solid excited by a strong heat pulse. *Phys. Rev. B* **14**, 4714–4723 (1976)
35. X.W. Wang, X. Xu, Thermoelastic wave induced by pulsed laser heating. *Appl. Phys. A* **73**, 107–114 (2001)
36. X.W. Wang, Thermal and thermomechanical phenomena in picosecond laser copper interaction. *J. Heat Transfer* **126**, 355–364 (2004)
37. S.I. Anisimov, B.L. Kapeliovich, T.L. Perel'man, Electron emission from metal surfaces exposed to ultrashort laser pulses. *Sov. Phys. JETP* **39**, 375–377 (1974)
38. J.G. Fujimoto, J.M. Liu, E.P. Ippen, N. Bloembergen, Femtosecond laser interaction with metallic tungsten and nonequilibrium electron and lattice temperatures. *Phys. Rev. Lett.* **53**, 1837–1840 (1984)
39. S.D. Brorson, J.G. Fujimoto, E.P. Ippen, Femtosecond electronic heat-transport dynamics in thin gold films. *Phys. Rev. Lett.* **59**, 1962–1965 (1987)
40. T.Q. Qiu, C.L. Tien, Short-pulse laser heating on metals. *Int. J. Heat Mass Transfer* **35**, 719–726 (1992)
41. T.Q. Qiu, C.L. Tien, Size effect on nonequilibrium laser heating of metal films. *J. Heat Transfer* **115**, 842–847 (1993)
42. T.Q. Qiu, T. Juhasz, C. Suarez, W.E. Bron, C.L. Tien, Femtosecond laser heating of multi-layer metals—II. Experiments. *Int. J. Heat Mass Transfer* **37**, 2799–2808 (1994)
43. J.L. Hostetler, A.N. Smith, D.M. Czajkowsky, P.M. Norris, Measurement of the electron-phonon coupling factor dependence on film thickness and grain size in Au, Cr, and Al. *Appl. Opt.* **38**, 3614–3620 (1999)
44. S. Link, C. Burda, Z.L. Wang, M.A. El-Sayed, Electron dynamics in gold and gold-silver alloy nanoparticles: The influence of a nonequilibrium electron distribution and the size dependence of the electron-phonon relaxation. *J. Chem. Phys.* **111**, 1255–1264 (1999)
45. A.N. Smith, P.M. Norris, Influence of intraband transition on the electron thermoreflectance response of metals. *Appl. Phys. Lett.* **78**, 1240–1242 (2001)
46. R.J. Stevens, A.N. Smith, P.M. Norris, Measurement of thermal boundary conductance of a series of metal-dielectric interfaces by the transient thermoreflectance techniques. *J. Heat Transfer* **127**, 315–322 (2005)
47. D.G. Cahill, K.E. Goodson, A. Majumdar, Thermometry and thermal transport in micro/nanoscale solid-state devices and structures. *J. Heat Transfer* **124**, 223–241 (2002)
48. D.G. Cahill, W.K. Ford, K.E. Goodson et al., Nanoscale thermal transport. *J. Appl. Phys.* **93**, 793–818 (2003)
49. J. Zhu, D.W. Tang, W. Wang, J. Liu, K.W. Holub, R. Yang, Ultrafast thermoreflectance techniques for measuring thermal conductivity and interface thermal conductance of thin films. *J. Appl. Phys.* **108**, 094315 (2010)
50. D.M. Riffe, X.Y. Wang, M.C. Downer et al., Femtosecond thermionic emission from metals in the space-charge-limited regime. *J. Opt. Soc. Am. B* **10**, 1424–1435 (1993)
51. A.N. Smith, J.L. Hostetler, P.M. Norris, Nonequilibrium heating in metal films: An analytical and numerical analysis. *Numer. Heat Transfer A* **35**, 859–874 (1999)
52. M. Li, S. Menon, J.P. Nibarger, G.N. Gibson, Ultrafast electron dynamics in femtosecond optical breakdown of dielectrics. *Phys. Rev. Lett.* **82**, 2394–2397 (1999)
53. L. Jiang, H.-L. Tsai, Energy transport and nanostructuring of dielectrics by femtosecond laser pulse trains. *J. Heat Transfer* **128**, 926–933 (2006)
54. L. Jiang, H.-L. Tsai, Plasma modeling for ultrashort pulse laser ablation of dielectrics. *J. Appl. Phys.* **100**, 023116 (2006)
55. Y. Ma, A two-parameter nondiffusive heat conduction model for data analysis in pump-probe experiments. *J. Appl. Phys.* **116**, 243505 (2014); *ibid*, Hotspot size-dependent thermal boundary conductance in nondiffusive heat conduction. *J. Heat Transfer* **137**, 082401 (2015)

56. G. Chen, Ballistic-diffusion heat-conduction equations. *Phys. Rev. Lett.* **86**, 2297–2300 (2001); *ibid.*, Ballistic-diffusive equations for transient heat conduction from nano to macroscales. *J. Heat Transfer* **124**, 320–328 (2002)
57. T. Klitsner, J.E. VanCleve, H.E. Fischer, R.O. Pohl, Phonon radiative heat transfer and surface scattering. *Phys. Rev. B* **38**, 7576–7594 (1988)
58. R.B. Peterson, Direct simulation of phonon-mediated heat transfer in a Debye crystal. *J. Heat Transfer* **116**, 815–822 (1994)
59. E.T. Swartz, P.O. Pohl, Thermal boundary resistance. *Rev. Mod. Phys.* **61**, 605–668 (1989)
60. W.A. Little, The transport of heat between dissimilar solids at low temperatures. *Can. J. Phys.* **37**, 334–349 (1959)
61. G. Chen and C.L. Tien, “Thermal conductivity of quantum well structures,” *J. Thermophys. Heat Transfer*, **7**, 311–318, 1993
62. G. Chen, Size and interface effects on thermal conductivity of superlattices and periodic thin-film structures. *J. Heat Transfer* **119**, 220–229 (1997)
63. G. Chen, Thermal conductivity and ballistic-phonon transport in the cross-plane direction of superlattices. *Phys. Rev. B* **57**, 14958–14973 (1998)
64. G. Chen, T. Zeng, Nonequilibrium phonon and electron transport in heterostructures and superlattices. *Microscale Thermophys. Eng.* **5**, 71–88 (2001)
65. T. Zeng, G. Chen, Phonon heat conduction in thin films: impacts of thermal boundary resistance and internal heat generation. *J. Heat Transfer* **123**, 340–347 (2001)
66. S. Sinha, K.E. Goodson, Review: multiscale thermal modeling in nanoelectronics. *Int. J. Multiscale Comp. Eng.* **3**, 107–133 (2005)
67. R.A. Escobar, S.S. Ghai, M.S. Jhon, C.H. Amon, Multi-length and time scale thermal transport using the lattice Boltzmann method with application to electronics cooling. *Int. J. Heat Mass Transfer* **49**, 97–107 (2006)
68. E.M. Sparrow, R.D. Cess, *Radiation Heat Transfer*, Augmented edn. (McGraw-Hill, New York, 1978)
69. M.F. Modest, *Radiative Heat Transfer*, 3rd edn. (Academic Press, New York, 2013)
70. T.J. Bright, Z.M. Zhang, Entropy generation in thin films evaluated from phonon radiative transport. *J. Heat Transfer* **132**, 101301 (2010)
71. H.B.G. Casimir, Note on the conduction of heat in crystal. *Physica* **5**, 495–500 (1938)
72. R.G. Deissler, Diffusion approximation for thermal radiation in gasses with jump boundary condition. *J. Heat Transfer* **86**, 240–245 (1964)
73. A. Malhotra, K. Kothari, M. Maldovan, Cross-plane thermal conduction in superlattices: Impact of multiple length scales on phonon transport. *J. Appl. Phys.* **125**, 044304 (2019)
74. K. Kothari, A. Malhotra, M. Maldovan, Cross-plane heat conduction in III–V semiconductor superlattices. *J. Phys. Condens. Matter* **31**, 345301 (2019)
75. M.M. Yovanovich, Four decades of research on thermal contact, gap, and joint resistance in microelectronics. *IEEE Trans. Compon. Packag. Technol.* **28**, 182–206 (2005)
76. R.J. Stoner, H.J. Maris, Kapitza conductance and heat flow between solids at temperatures from 50 to 300 K. *Phys. Rev. B* **48**, 16373–16387 (1993)
77. R.S. Prasher and P.E. Phelan, “Review of thermal boundary resistance of high-temperature superconductors,” *J. Supercond.*, **10**, 473–484, 1997
78. P.E. Phelan, Application of diffuse mismatch theory to the prediction of thermal boundary resistance in thin-film high- $T_c$  superconductors. *J. Heat Transfer* **120**, 37–43 (1998)
79. L. De Bellis, P.E. Phelan, R.S. Prasher, Variations of acoustic and diffuse mismatch models in predicting thermal-boundary resistance. *J. Thermophys. Heat Transfer* **14**, 144–150 (2000)
80. A. Majumdar, Effect of interfacial roughness on phonon radiative heat conduction. *J. Heat Transfer* **113**, 797–805 (1991)
81. A. Majumdar, P. Reddy, Role of electron–phonon coupling in thermal conductance of metal–nonmetal interfaces. *Appl. Phys. Lett.* **84**, 4768–4770 (2004)
82. A. Giri, P.E. Hopkins, A review of experimental and computational advances in thermal boundary conductance and nanoscale thermal transport across solid interfaces. *Adv. Func. Mater.* **2019**, 1903857 (2019)

83. S. Mazumdar, A. Majumdar, Monte Carlo study of phonon transport in solid thin films including dispersion and polarization. *J. Heat Transfer* **123**, 749–759 (2001)
84. Q. Hao, G. Chen, M.-S. Jeng, Frequency-dependent Monte Carlo simulations of phonon transport in two-dimensional porous silicon with aligned pores. *J. Appl. Phys.* **106**, 114321 (2009)
85. J.-P.M. Péraud, C.D. Landon, N.G. Hadjiconstantinou, Monte Carlo methods for solving the Boltzmann transport equation. *Annu. Rev. Heat Transfer* **17**, 205–265 (2014)
86. A. Nabovati, D.P. Sellan, C.H. Amon, On the lattice Boltzmann method for phonon transport. *J. Comput. Phys.* **230**, 5864–5876 (2011)
87. S.R. Phillpot, P.K. Schelling, P. Keblinski, Phonon wave-packet dynamics at semiconductor interfaces by molecular-dynamics simulation. *Appl. Phys. Lett.* **80**, 2484–2486 (2002); *ibid*, Interfacial thermal conductivity: Insights from atomic level simulation. *J. Mater. Sci.* **40**, 3143–3148 (2005)
88. C.-J. Twu, J.-R. Ho, Molecular-dynamics study of energy flow and the Kapitza conductance across an interface with imperfection formed by two dielectric thin films. *Phys. Rev. B* **67**, 205422 (2003)
89. H. Zhong, J.R. Lukes, Interfacial thermal resistance between carbon nanotubes: Molecular dynamics simulations and analytical thermal modeling. *Phys. Rev. B* **74**, 125403 (2006)
90. R.J. Stevens, L.V. Zhigilei, P.M. Norris, Effects of temperature and disorder on thermal boundary conductance at solid-solid interfaces: non-equilibrium molecular dynamics simulations. *Int. J. Heat Mass Transfer* **50**, 3977–3989 (2007)
91. E.S. Landry, A.J.H. McGaughey, Thermal boundary resistance predictions from molecular dynamics simulations and theoretical calculations. *Phys. Rev. B* **80**, 165304 (2009)
92. Y. Chalopin, K. Esfarjani, A. Henry, S. Volz, G. Chen, Thermal interface conductance in Si/Ge superlattices by equilibrium molecular dynamics. *Phys. Rev. B* **85**, 195302 (2012)
93. S. Merabia, K. Termentzidis, Thermal conductance at the interface between crystals using equilibrium and nonequilibrium molecular dynamics. *Phys. Rev. B* **86**, 094303 (2012)
94. Z. Liang, M. Hu, Tutorial: Determination of thermal boundary resistance by molecular dynamics simulations. *J. Appl. Phys.* **123**, 191101 (2018)
95. F. VanGessel, J. Peng, P.W. Chung, A review of computational phononics: the bulk, interfaces, and surfaces. *J. Mater. Sci.* **53**, 5641–5683 (2018)
96. S. Datta, Nanoscale device modeling: the Green’s function method. *Superlattices Microstruct.* **28**, 253–278 (2000)
97. N. Mingo, L. Yang, Phonon transport in nanowires coated with an amorphous material: an atomistic Green’s function approach. *Phys. Rev. B* **68**, 245406 (2003)
98. W. Zhang, T.S. Fisher, N. Mingo, Simulation of interfacial phonon transport in Si–Ge heterostructures using an atomistic Green’s function method. *J. Heat Transfer* **129**, 483–491 (2007); *ibid*, The atomistic Green’s function method: an efficient simulation approach for nanoscale phonon transport. *Numerical Heat Transfer B* **51**, 333–349 (2007)
99. S. Sadasivam, Y. Che, Z. Huang, L. Chen, S. Kumar, T.S. Fisher, The atomistic Green’s function method for interfacial phonon transport. *Annu. Rev. Heat Transfer* **17**, 89–145 (2014)
100. A. Ozpineci, S. Ciraci, Quantum effects of thermal conductance through atomic chains. *Phys. Rev. B* **63**, 125415 (2001)
101. Z.-Y. Ong, G. Zhang, Efficient approach for modeling phonon transmission probability in nanoscale interfacial thermal transport. *Phys. Rev. B* **91**, 174302 (2015)
102. L. Yang, B. Latour, A.J. Minnich, Phonon transmission at crystalline-amorphous interfaces studied using mode-resolved atomistic Green’s functions. *Phys. Rev. B* **97**, 205306 (2018)
103. D.A. Young, H.J. Maris, Lattice-dynamical calculation of the Kapitza resistance between fcc lattices. *Phys. Rev. B* **40**, 3685–3693 (1989)
104. H. Zhao, J.B. Freund, Lattice-dynamical calculation of phonon scattering at ideal Si–Ge interfaces. *J. Appl. Phys.* **97**, 024903 (2005)
105. S. Sadasivam, N. Ye, J.P. Feser, J. Charles, K. Miao, T. Kubis, T.S. Fisher, Thermal transport across metal silicide-silicon interfaces: First-principles calculations and Green’s function transport simulations. *Phys. Rev. B* **95**, 085310 (2017)

106. Z. Tian, K. Esfarjani, G. Chen, Green's function studies of phonon transport across Si/Ge superlattices. *Phys. Rev. B* **89**, 235307 (2014)
107. Z. Yan, L. Chen, M. Yoon, S. Kumar, Phonon transport at the interfaces of vertically stacked graphene and hexagonal boron nitride heterostructures. *Nanoscale* **8**, 4037 (2016)
108. J. Lai, A. Majumdar, Concurrent thermal and electrical modeling of sub-micrometer silicon devices. *J. Appl. Phys.* **79**, 7353–7361 (1996)
109. P.G. Sverdrup, Y.S. Ju, K.E. Goodson, Sub-continuum simulation of heat conduction in silicon-on-insulator transistors. *J. Heat Transfer* **123**, 130–137 (2001)
110. S. Sinha, E. Pop, R.W. Dutton, K.E. Goodson, Non-equilibrium phonon distribution in sub-100 nm silicon transistors. *J. Heat Transfer* **128**, 638–647 (2006)
111. C.D.S. Brites, P.P. Lima, N.J.O. Silva, A. Millán, V.S. Amaral, F. Palacio, L.D. Carlos, Thermometry at the nanoscale. *Nanoscale* **4**, 4799–4829 (2012)
112. X.W. Wang, *Experimental Micro/Nanoscale Thermal Transport* (Wiley, New York, 2012)
113. A.J. McNamara, Y. Joshi, Z.M. Zhang, Characterization of nanostructured thermal interface materials—a review. *Int. J. Thermal Sci.* **62**, 2–11 (2012)
114. G. Chen, Probing nanoscale heat transfer phenomena. *Annu. Rev. Heat Transfer* **16**, 1–8 (2013)
115. D. Zhao, X. Qian, X. Gu, S.A. Jajja, R. Yang, Measurement techniques for thermal conductivity and interfacial thermal conductance of bulk and thin film materials. *J. Electron. Package* **138**, 040802 (2016)
116. Z.M. Zhang, Surface temperature measurement using optical techniques. *Annu. Rev. Heat Transfer* **11**, 351–411 (2000)
117. B. Abad, D.-A. Borca-Tasciuc, M.S. Martin-Gonzalez, Non-contact methods for thermal properties measurement. *Renew. Sustain. Energy Rev.* **76**, 1348–1370 (2017)
118. A.C. Jones, B.T. O'Callahan, H.U. Yang, M.B. Raschke, The thermal near-field: coherence, spectroscopy, heat-transfer, and optical forces. *Prog. Sur. Sci.* **88**, 349–392 (2013)
119. K.E. Goodson, Y.S. Ju, Heat conduction in novel electronic films. *Annu. Rev. Mater. Sci.* **29**, 261–293 (1999)
120. K. Park, G.L.W. Cross, Z.M. Zhang, W.P. King, Experimental investigation on the heat transfer between a heated microcantilever and a substrate. *J. Heat Transfer* **130**, 102401 (2008)
121. D. G. Cahill and R. O. Pohl, "Thermal conductivity of amorphous solids above the plateau," *Phys. Rev. B*, **35**, 4067–4073, 1987
122. D.G. Cahill, H.E. Fischer, T. Klitsner, E.T. Swartz, R.O. Pohl, Thermal conductivity of thin films: measurements and understanding. *J. Vac. Sci. Technol. A* **7**, 1259–1266 (1989)
123. D.G. Cahill, Thermal conductivity measurement from 30 K to 750 K: the 3-omega method. *Rev. Sci. Instrum.* **61**, 802–808 (1990)
124. C. Dames, Measuring the thermal conductivity of thin films: 3 omega and related electrothermal methods. *Annu. Rev. Heat Transfer* **16**, 7–49 (2013)
125. S. Kommandur, S.K. Yee, A suspended 3-omega technique to measure the anisotropic thermal conductivity of semiconducting polymers. *Rev. Sci. Instrum.* **89**, 114905 (2018)
126. L. Shi, D. Li, C. Yu, W. Jang, D. Kim, Z. Yao, P. Kim, A. Majumdar, Measuring thermal and thermoelectric properties of one-dimensional nanostructures using a microfabricated device. *J. Heat Transfer* **125**, 881–888 (2003)
127. P. Kim, L. Shi, A. Majumdar, P.L. McEuen, Thermal transport measurements of individual multiwalled nanotubes. *Phys. Rev. Lett.* **87**, 215502 (2001)
128. C. Yu, L. Shi, Z. Yao, D. Li, A. Majumdar, Thermal conductance and thermopower of an individual single-wall carbon nanotube. *Nano Lett.* **5**, 1842–1846 (2005)
129. A. Mavrokefalos, M.T. Pettes, F. Zhou, L. Shi, Four-probe measurements of the in-plane thermoelectric properties of nanofilms. *Rev. Sci. Instrum.* **78**, 034901 (2007)
130. A. Weathers, L. Shi, Thermal transport measurement techniques for nanowires and nanotubes. *Annu. Rev. Heat Transfer* **16**, 101–134 (2013)
131. M. Fujii, X. Zhang, H. Xie, H. Ago, K. Takahashi, T. Ikuta, H. Abe, T. Shimizu, Measuring the thermal conductivity of a single carbon nanotube. *Phys. Rev. Lett.* **95**, 065502 (2005)

132. J. Kim, E. Ou, D.P. Sellan, L. Shi, A four-probe thermal transport measurement method for nanostructures. *Rev. Sci. Instrum.* **86**, 044901 (2015)
133. J. Kim, D.A. Evans, D.P. Sellan, O.M. Williams, E. Ou, A.H. Cowley, L. Shi, Thermal and thermoelectric transport measurements of an individual boron arsenide microstructure. *Appl. Phys. Lett.* **108**, 201905 (2016)
134. A. Majumdar, Scanning thermal microscopy. *Annu. Rev. Mater. Sci.* **29**, 505–585 (1999)
135. A. Majumdar, J. P. Carrejo, J. Lai, Thermal imaging using the atomic force microscope. *Appl. Phys. Lett.* **62**, 2501–2503 (1993)
136. A. Majumdar, J. Lai, M. Chandrachood, O. Nakabeppu, Y. Wu, J. Shi, Thermal imaging by atomic force microscopy using thermocouple cantilever probes. *Rev. Sci. Instrum.* **66**, 3584–3592 (1995)
137. C.C. Williams, H.K. Wickramasinghe, Scanning thermal profiler. *Appl. Phys. Lett.* **49**, 1587–1589 (1986)
138. A. Majumdar, J. Varesi, Nanoscale temperature distribution measured by scanning Joule expansion microscopy. *J. Heat Transfer* **120**, 297–305 (1998)
139. S.P. Gurrum, W.P. King, Y.K. Joshi, K. Ramakrishna, Size effect on the thermal conductivity of thin metallic films investigated by scanning Joule expansion microscopy. *J. Heat Transfer* **130**, 082403 (2008)
140. K.L. Grosse, M.-H. Bae, F. Lian, E. Pop, W.P. King, Nanoscale Joule heating, Peltier cooling and current crowding at graphene-metal contacts. *Nat. Nanotech.* **6**, 287–290 (2011)
141. T. Borca-Tasciuc, Scanning probe methods for thermal and thermoelectric property measurements. *Annu. Rev. Heat Transfer* **16**, 211–258 (2013)
142. S. Gomès, A. Assy, P.-O. Chapuis, Scanning thermal microscopy: a review. *Phys. Status Solidi A* **212**, 477–494 (2015)
143. K. Kim, J. Chung, G. Hwang, O. Kwon, J.S. Lee, Quantitative measurement with scanning thermal microscope by preventing the distortion due to the heat transfer through the air. *ACS Nano* **11**, 8700–8709 (2011)
144. H.F. Hamann, Y.C. Martin, H.K. Wickramasinghe, Thermally assisted recording beyond traditional limits. *Appl. Phys. Lett.* **84**, 810–812 (2004)
145. W.P. King, T.W. Kenny, K.E. Goodson et al., Atomic force microscope cantilevers for combined thermomechanical data writing and reading. *Appl. Phys. Lett.* **78**, 1300–1302 (2001)
146. J. Lee, T. Beechem, T. L. Wright, B. A. Nelson, S. Graham, W. P. King, Electrical, thermal, and, mechanical characterization of silicon microcantilever heaters. *J. Microelectromech. Syst.* **15**, 1644 (2007)
147. J. Lee, T.L. Wright, M.R. Abel et al., Thermal conduction from microcantilever heaters in partial vacuum. *J. Appl. Phys.* **101**, 014906 (2007)
148. K. Park, J. Lee, Z.M. Zhang, W.P. King, Frequency-dependent electrical and thermal response of heated atomic force microscope cantilevers. *J. Microelectromech. Syst.* **16**, 213–222 (2007)
149. K. Park, A. Marchenkov, Z.M. Zhang, W.P. King, Low temperature characterization of heated microcantilevers. *J. Appl. Phys.* **101**, 094504 (2007)
150. W.P. King, B. Bhatia, J.R. Felts, H.J. Kim, B. Kwon, B. Lee, S. Somnath, M. Rosenberger, Heated atomic force microscope cantilevers and their applications. *Annu. Rev. Heat Transfer* **16**, 287–326 (2013)
151. A.J. Schmidt, X. Chen, G. Chen, Pulse accumulation, radial heat conduction, and anisotropic thermal conductivity in pump-probe transient thermoreflectance. *Rev. Sci. Instrum.* **79**, 114802 (2008)
152. A.J. Minnich, Measuring phonon mean free paths using thermal conductivity spectroscopy. *Annu. Rev. Heat Transfer* **16**, 183–210 (2013)
153. J. Zhu, H. Park, J.-Y. Chen et al., Revealing the origins of 3D anisotropic thermal conductivities of black phosphorus. *Adv. Electron. Mater.* **2**, 1600040 (2016)
154. P. Jiang, X. Qian, R. Yang, Tutorial: time-domain thermoreflectance (TDTR) for thermal property characterization of bulk and thin film materials. *J. Appl. Phys.* **124**, 161103 (2018)

155. Z. Cheng, T. Bougher, T. Bai et al., Probing growth-induced anisotropic thermal transport in high-quality CVD diamond membranes by multifrequency and multiple-spot-size time-domain thermoreflectance. *ACS Appl. Mater. Interfaces*, **10**, 4808–4815 (2018)
156. S. Huxtable, D.G. Cahill, V. Fauconnier, J.O. White, J.-C. Zhao, Thermal conductivity imaging at micrometre-scale resolution for combinatorial studies of materials. *Nat. Mater.* **3**, 298–301 (2004)
157. D.G. Cahill, Analysis of heat flow in layered structures for time-domain thermoreflectance. *Rev. Sci. Instrum.* **75**, 5119–5122 (2004)
158. J. Jeong, X. Meng, A. K. Rockwell et al., Picosecond transient thermoreflectance for thermal conductivity characterization. *Nanoscale Microscale Thermophys. Eng.* **23**, 211–221 (2019)
159. P.M. Norris, A.P. Caffrey, R.J. Stevens, J.M. Klopff, J.T. McLeskey, A.N. Smith, Femtosecond pump–probe nondestructive examination of materials. *Rev. Sci. Instrum.* **74**, 400–406 (2003)
160. K.E. Goodson, M. Asheghi, Near-field optical thermometry. *Microscale Thermophys. Eng.* **1**, 225–235 (1997)
161. D. Seto, R. Nikka, S. Nishio, Y. Taguchi, T. Saiki, Y. Nagasaka, Nanoscale optical thermometry using a time-correlated single-photon counting in an illumination-collection mode. *Appl. Phys. Lett.* **110**, 033109 (2017)
162. M.E. Siemens, Q. Li, R. Yang, K.A. Nelson, E.H. Anderson, M.M. Murnane, H.C. Kapteyn, Quasi-ballistic thermal transport from nanoscale interfaces observed using ultrafast coherent soft X-ray beams. *Nat. Mater.* **9**, 26–30 (2010)
163. T. Favalaro, J.-H. Bahk, A. Shakouri, Characterization of the temperature dependence of the thermoreflectance coefficient for conductive thin films. *Rev. Sci. Instrum.* **86**, 024903 (2015)
164. C. Wei, X. Zheng, D.G. Cahill, J.-C. Zhao, Invited article: Micron resolution spatially resolved measurement of heat capacity using dual-frequency time-domain thermoreflectance. *Rev. Sci. Instrum.* **84**, 071301 (2013)
165. P.E. Hopkins, C.M. Reinke, M.F. Su, R.H. Olsson III, E.A. Shaner, Z.C. Leseman, J.R. Serrano, L.M. Phinney, I. El-Kady, Reduction in the thermal conductivity of single crystalline silicon by phononic crystal patterning. *Nano Lett.* **11**, 107–112 (2011)
166. M.R. Wagner, B. Graczykowski, J.S. Reparaz et al., Two-dimensional photonic crystals: Disorder matters. *Nano Lett.* **16**, 5661–5668 (2016)
167. X. Wang, T. Mori, I. Kuzmych-Ianchuk, Y. Michiue, K. Yubuta, T. Shishido, Y. Grin, S. Okada, D.G. Cahill, Thermal conductivity of layered borides: The effect of building defects on the thermal conductivity of TmAlB<sub>4</sub> and the anisotropic thermal conductivity of AlB<sub>2</sub>. *APL Mater.* **2**, 046113 (2014)
168. J. Liu, G.-M. Choi, D.G. Cahill, Measurement of the anisotropic thermal conductivity of molybdenum disulfide by the time-resolved magneto-optic Kerr effect. *J. Appl. Phys.* **116**, 233107 (2014)
169. A. J. Schmidt, R. Cheaito, M. Chiesa, A frequency-domain thermoreflectance method for the characterization of thermal properties. *Rev. Sci. Instrum.* **80**, 094901 (2009); *ibid*, Characterization of thin metal films via frequency-domain thermoreflectance. *J. Appl. Phys.* **107**, 024908 (2010)
170. K.T. Regner, D.P. Sellan, Z. Su, C.H. Amon, A.J.H. McGaughey, J.A. Malen, Broadband phonon mean free path contributions to thermal conductivity measured using frequency domain thermoreflectance. *Nat. Commun.* **4**, 1640 (2013)
171. D. Rodin, S.K. Yee, Simultaneous measurement of in-plane and through-plane thermal conductivity using beam-offset frequency domain thermoreflectance. *Rev. Sci. Instrum.* **88**, 014902 (2017)
172. J. Johnson, A. A. Maznev, J. Cuffe, J. K. Eliason, A. J. Minnich, T. Kehoe, C. M. Sotomayor Torres, G. Chen, K. A. Nelson, Direct measurement of room-temperature nondiffusive thermal transport over micron distances in a silicon membrane. *Phys. Rev. Lett.* **110**, 025901 (2013)
173. J. Cuffe, J.K. Eliason, A.A. Maznev et al., Reconstructing phonon mean-free-path contributions to thermal conductivity using nanoscale membranes. *Phys. Rev. B* **91**, 245423 (2015)
174. A. Vega-Flick, R.A. Duncan, J.K. Eliason et al., Thermal transport in suspended silicon membranes measured by laser-induced transient gratings. *AIP Adv.* **6**, 120903 (2016)